

Mapping the thermal structure of southern Africa from Curie depth estimates based on wavelet analysis of magnetic data with uncertainties

Mohamed Sobh¹, Christian Gerhards², Hans-Jürgen Götze³, and Islam Fadel⁴

¹Institute of Geophysics and Geoinformatics, TU Bergakademie Freiberg, Germany

²Institute of Geophysics and Geoinformatics

³Institute of Geosciences, Christian-Albrechts-University Kiel

⁴University of Twente

November 23, 2022

Abstract

Surface heat flow provides essential information on the thermal state and thickness of the lithosphere. Southern Africa is a mosaic of the best-preserved and exposed crustal blocks, assembled in the early late Archean and then modified by a series of major tectono-thermal events, both of Precambrian and Phanerozoic. Understanding the thermal and compositional structure of the southern African lithosphere provides crucial information for the actual causes, processes of lithospheric stability, and modification. Temperature plays a major role in the distribution of the long-wavelength crustal magnetic anomalies. Curie depth, interpreted as the depth to 580°C , provides a valuable constraint on the thermal structure of the lithosphere. Due to the sparse distribution of surface heat flow data, we examine the degree to which the thermal structure of the crust can be constrained from the Curie depth in southern Africa. The Curie depth is estimated from magnetic anomaly data using spectral methods in combination wavelet analysis; a Bayesian approach is applied to address the uncertainty. Subsequently, the obtained Curie depth is used to estimate the surface heat flow, and the outcome is compared to available heat flow measurements. Unlike other cratonic regions, the shallowest Curie depth and low effective elastic thickness values observed over the Kaapvaal Craton suggest thermal reworking of the cratonic lithosphere in this region.

Mapping the thermal structure of southern Africa from Curie depth estimates based on wavelet analysis of magnetic data with uncertainties

M. Sobh¹, C. Gerhards¹, I. Fadel², and H.-J. Götze³

¹Institute of Geophysics and Geoinformatics, TU Bergakademie Freiberg, Germany

²Faculty of Geo-Information Science and Earth Observation, University of Twente, Enschede, Netherlands

³Institute of Geoscience, Christian-Albrechts-University Kiel, Otto-Hahn-Platz 1, D-24118 Kiel, Germany

Key Points:

- Depth to the bottom of the magnetized source over southern Africa via power spectral methods and wavelet transforms are estimated.
- Estimation of heat flow and its uncertainty based on Curie depth are estimated within a Bayesian framework.
- The shallow magmatic provinces along the Kalahari magnetic lineament lead to an underestimation of the Curie depths.

Corresponding author: Mohamed Sobh, Mohamed.Sobh@geophysik.tu-freiberg.de

Abstract

Surface heat flow provides essential information on the thermal state and thickness of the lithosphere. Southern Africa is a mosaic of the best-preserved and exposed crustal blocks, assembled in the early late Archean and then modified by a series of major tectono-thermal events, both of Precambrian and Phanerozoic. Understanding the thermal and compositional structure of the southern African lithosphere provides crucial information for the actual causes, processes of lithospheric stability, and modification. Temperature plays a major role in the distribution of the long-wavelength crustal magnetic anomalies. Curie depth, interpreted as the depth to 580°C, provides a valuable constraint on the thermal structure of the lithosphere.

Due to the sparse distribution of surface heat flow data, we examine the degree to which the thermal structure of the crust can be constrained from the Curie depth in southern Africa. The Curie depth is estimated from magnetic anomaly data using spectral methods in combination wavelet analysis; a Bayesian approach is applied to address the uncertainty. Subsequently, the obtained Curie depth is used to estimate the surface heat flow, and the outcome is compared to available heat flow measurements. Unlike other cratonic regions, the shallowest Curie depth and low effective elastic thickness values observed over the Kaapvaal Craton suggest thermal reworking of the cratonic lithosphere in this region.

Plain Language Summary

The thermal state and thickness of the lithosphere are reflected, among other quantities, in the surface heat flow. While heat flow data are rather sparse, magnetic anomaly maps are widely available and allow, under certain conditions, the estimation of the bottom of the magnetized layer within the lithosphere. Latter can be associated with the 580°C-isotherm (frequently called the Curie depth), therefore allowing inferences on the thermal state of the lithosphere from magnetic data.

Here, we use classical power spectral methods in combination with wavelet analysis and Bayesian methods to estimate the Curie depth and its uncertainty from magnetic anomaly maps, and subsequently, use it to estimate the surface heat flow over southern Africa. Comparison with the sparsely available measured heat flow allows us to assess the quality of the estimation and to interpret it with respect to the lithospheric structure. Southern Africa is particularly suitable for such a study due to its well-preserved and well-studied crustal blocks. One outcome of our study is, e.g., that the shallow Curie depths observed over the Kaapvaal Craton suggest a thermal reworking of the old lithospheric structures in this region.

1 Introduction

Estimating the spatial variations in the temperature within the Earth is important to constrain the thermal structure and the rheology of the lithosphere (Audet & Gosselin, 2019). Curie depth estimates, which correspond to the depth where crustal rocks reach their Curie temperature ($\sim 580^\circ\text{C}$ for magnetite; Dunlop & Özdemir (2001)) give independent temperature constraints over an area where magnetic anomaly data are available. Above the Curie temperature, rocks lose their ability to maintain ferromagnetic magnetization (Haggerty, 1978) and become paramagnetic. Therefore, we identify the Curie depth with the depth of the magnetized crust (although the Curie depth reflects a transition zone rather than an exact depth (Haggerty, 1978)). This can provide information on crustal temperatures at depths not accessible by boreholes (Andrés et al., 2018) and, consequently, yields a valuable constraint for geothermal heat flow (Kaban et al., 2014).

The thickness and depth to the base of the magnetized crust (Curie depth) is reflected in the wavenumber content of the magnetic anomaly data. Under certain assumptions, like a fractal magnetization model, the magnetic thickness and depth can be estimated directly from the radially averaged power spectrum of the magnetic anomaly (Bouligand et al., 2009; Maus et al., 1997). Various methods have been proposed in that direction and have been applied to many regions of the Earth. Typically, magnetic anomaly data are interpolated, gridded, and processed by moving windows approaches to suit such a spectral setup. Li et al. (2017) presents a global Curie depth model based on magnetic anomaly but does not provide the estimated uncertainty of Curie depth. Here, we use a 2-D wavelet approach, in combination with the classical power spectrum setup, where wavelets at different scales are convolved with the entire magnetic anomaly grid to estimate the wavenumber content of the data at particular locations (Swain & Kirby, 2003; Kirby & Swain, 2014; Pérez-Gussinyé et al., 2009; Gaudreau et al., 2019). This avoids the segmentation of the signal into finite-size windows. Additionally, we incorporate a Bayesian framework in order to supply uncertainties for the obtained Curie depth estimates (Mather & Fullea, 2019; Mather & Delhaye, 2019).

Alternative approaches to classical Curie depth estimation via spectral methods are currently under development (Ebbing, Szwillus, & Dilixiati, 2021). Here we stick to the classical approach but combine it with wavelets and a Bayesian setup to address and quantify at least some of its shortcomings. The focus of the paper is the interpretation of the calculated results of the Curie depth and heat flow estimates in terms of the geological and tectonic setting in southern Africa. We also provide uncertainty metrics to inform the interpretation of the resulting map and its further use.

Despite the importance of Curie depth estimation from magnetic data, the question arises whether the spectral techniques can provide reliable depth estimates and if these estimates represent the Curie isotherms or a structural boundary (Ebbing et al., 2009). This is a concern particularly in the stable cratonic lithosphere and when the tectonic domain is overprinted by magmatic intrusions. In the course of the paper, we interpret the estimated Curie depths over southern Africa in terms of geology and tectonics of the region, as well as in the context of the Moho and available heat flow data. Considering the Curie depth as a proxy to the lithospheric thermal structure, we use it to compute the temperature distribution within the crust. Due to limited heat flow values based on direct measurements, and the need for better estimates and best constrain the spatial variation of heat flow, indirect method is applying here. This helps to constrain models of thermally controlled physical properties and processes, particularly where heat flow measurements are sparse (Li et al., 2017). We validate our predictions of geothermal heat flow across southern Africa against surface heat flow data to examine the variations and controls of the crustal thermal architecture, while accepting that the uncertainties remain large. The plethora of publicly available data sets over southern Africa make it an ideal site to study and map the variations of Curie depth and its implications.

1.1 The Tectonic Settings of Southern Africa

The southern African tectonics consists of diverse tectonic terrains with unique characteristics (cf. White-Gaynor et al. (2020) and Figure 1): (1) The main tectonic units are the Archean Cratons that represent the ancient and stable core of the shield. (2) The Cratons are surrounded by mobile belts that were under continuous deformation of rifting and accretion during the different orogenic cycles during the Archean, Proterozoic, and continued during the Phanerozoic. (3) Within the Craton and the mobile belts Precambrian terrains exist that has experienced Phanerozoic compressional tectonics, flood basalt volcanism, rifting, and plateau uplifting. On top of these diverse

tectonic units exist sedimentary basins that have developed during the Neoproterozoic and early Palaeozoic times with depth that reach up to 15 km (Fadel et al., 2018)

There are three main Cratons within the study area. The Kaapvaal and Zimbabwe Cratons formed in the Mesoarchean to Neoarchean and mainly consist of granite-greenstone terranes (de Wit et al., 1992). The Limpopo Belt suture the Kaapvaal and the Zimbabwe cratons and the three units together form the greater Kalahari Craton (de Wit et al., 1992). The Limpopo Belt was formed during the Neoarchean collision between the Zimbabwe and Kaapvaal craton. The last major tectono-thermal events that affected the Kalahari Craton were, respectively, the emplacement of the Great Dike Karoo in the Zimbabwe craton in the late Neoarchean (c. 2.6 Ga) (Jelsma & Dirks, 2002), and the formation of the Bushveld igneous complex during the Paleoproterozoic (c. 2.1 Ga) within the Kaapvaal craton (Figure 1; Olsson et al. (2010)). To the northwest of the study area exists the Congo Craton that consists of Archean and Paleoproterozoic rock units that with the oldest record at the northwestern block was formed during the Mesoarchean (Begg et al., 2009; Ernst et al., 2013). The Congo Craton and the Sao Francisco Craton in South America amalgamated together as one unit during the Paleoproterozoic (2.0 Ga) until the breakup of Africa and South America in the Mesozoic (130 Ma; Ernst et al. (2013)). The Rehoboth is one of the poorer-defined regions in the study area with an Archean Nuclei (Van Schijndel et al., 2011).

Southern Africa was subjected to continental growth during the Proterozoic due to the accretion of younger blocks to the Archean terranes (Figure 1). A significant part of the Rehoboth province was formed and aggregated around the Archean Nuclei during the Paleoproterozoic (Van Schijndel et al., 2011). Then, the Kheis Belt and Rehoboth Province accreted during the Paleoproterozoic to the western margin of the Kaapvaal Craton (R. Hanson, 2003). After that, the Namaqua-Natal Mobile Belt was formed and surrounded the southern margins of the Rehoboth province and Kaapvaal Craton in the Mesoproterozoic (c. 1.2-1.0 Ga; McCourt et al. (2001)). From the northwest to the center of the study area exists the Magondi-Okwa-Kheis belts that are formed during the Paleoproterozoic (2.0-1.8) and accreted due to the Eburnean Orogeny to the northwestern border of the Kalahari Craton (Begg et al., 2009)

Within the study area, there are two major Pan-African orogenic belts. The Mozambique Belt originated in the eastern part of the study region during the final assembly of Gondwana, c. 841–632 Ma (R. Hanson, 2003). During the collision of the larger Kalahari Craton and the Congo Craton c. 580–500 Ma, Damara Ghanzi-Chobe belt (hence called Damaran Mobile Belt) emerged in the northwest. The original breakup of Gondwana corresponded with the creation of the c. 180 Ma Karoo major igneous province and the rifting of the Karoo over southern Africa (Duncan et al., 1997). The Cenozoic era is characterized by the emergence of the initial rifts caused by the spread of the EARS to the South. Seismically active fault systems indicate that rifting is beginning in the Okavango Rift Zone (ORZ) in northern Botswana (Schmitz & Bowring, 2003), with the East African Rift System potentially extending to central Botswana as well (Fadel et al., 2020). The different tectonic domains with different tectonic history and different ages varying from old Cratonic lithosphere, mobile belts and Phanerozoic rifting and flood basalt volcanism combined with the plateau uplift and the terminus of the East African rift system make southern Africa open laboratory to study and map the variations of Curie depth along different domains with different tectonic history and current thermal status.

2 Methodology

There are two steps applied in the course of proposed workflow: first, the Curie depth estimation from magnetic data (described in Section 2.1) and, subsequently,

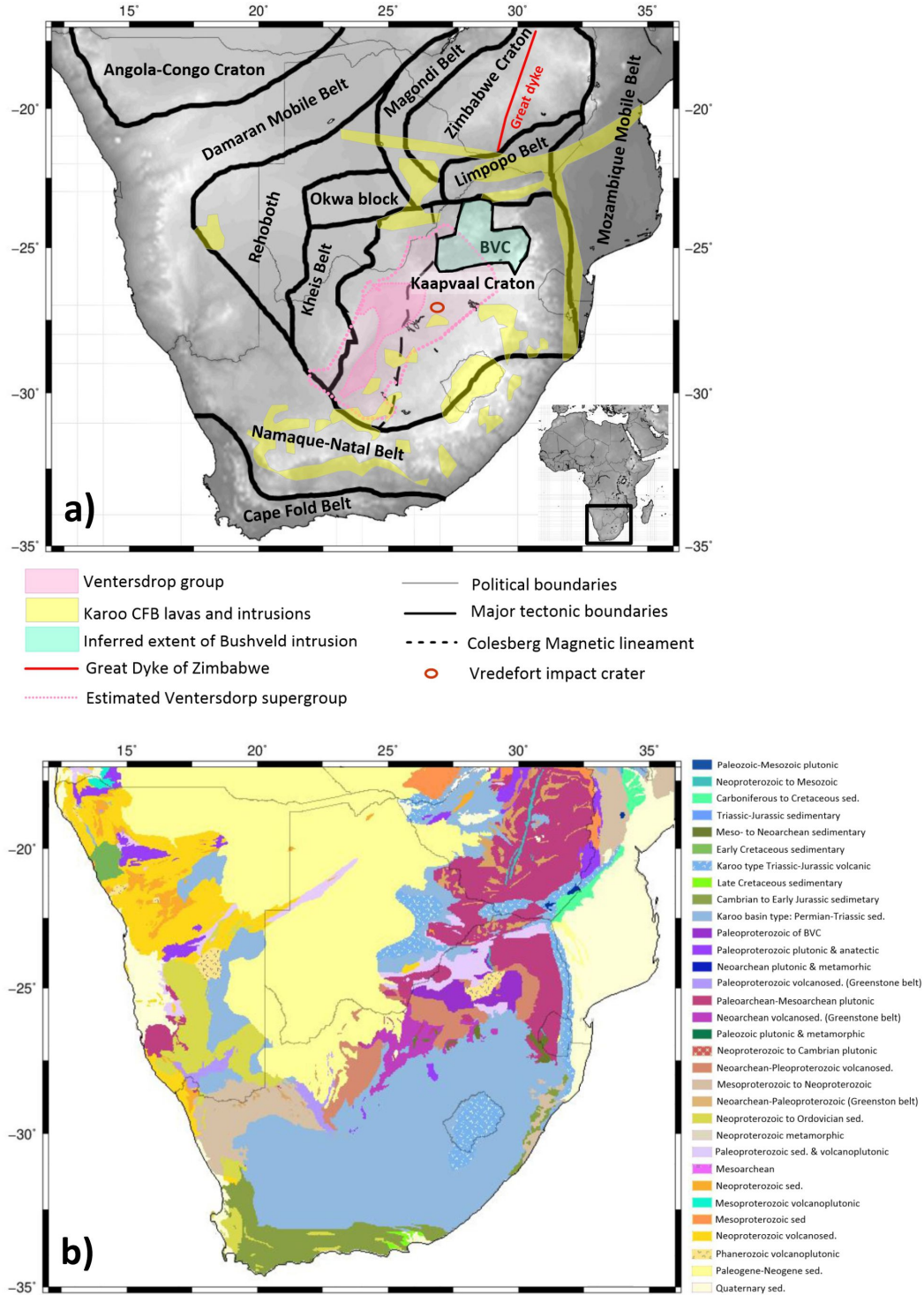


Figure 1. (a) Simplified tectonic map of the southern Africa terranes overlain with the gray shaded topography. BVC = Bushveld Igneous Complex. Tectonic boundaries (de Wit et al., 1992; Goodwin, 1996); the Neoproterozoic Venterdrop magmatic province (Schmitz & Bowring, 2003), the inferred extent of the Bushveld Igneous Complex (Campbell et al., 1983), and of the Umkondo continental flood basalt province (CFB) (R. E. Hanson et al., 2004); major Karoo lavas and outcrops (Riley et al., 2006). (b) Tectonic ages of the southern Africa, with the permission of OneGeology (<http://portal.onegeology.org/OnegeologyGlobal/>).

the modelling of geothermal heat flow based on Curie depth constraints (described in Section 2.2).

2.1 Curie Depth Estimation

Various spectral methods have been proposed and applied to estimate depth to the bottom of the lithospheric magnetization (e.g., Tanaka et al. (1999); Bouligand et al. (2009); Salem et al. (2014); Maus et al. (1997); Chopping & Kennett (2013); Li et al. (2017); Gaudreau et al. (2019)). This depth will be identified with the Curie depth throughout the remainder of this paper. We refer to the recent overview by Núñez et al. (2021) for a comparison of some of the approaches. In the following, we rather briefly describe the specific setup used in our approach.

We assume that the magnetized layer of the lithosphere is confined between two surfaces at depths z_t (top of the magnetized layer) and z_b (bottom of the magnetized layer). The thickness of the layer is denoted by $\Delta z = z_b - z_t$. Within this layer, we assume the magnetization to be of self-similar nature, described by a fractal parameter β . This yields that the power spectrum Φ_M of the underlying magnetization is of the form

$$\Phi_M(k) = Ck^{-\beta}, \quad (1)$$

where $k = |\mathbf{k}|$ and $\mathbf{k} = (k_x, k_y, k_z)$ is the wavenumber; C is some proportionality constant. Given these assumptions, the radial power spectrum Φ of the magnetic anomaly corresponding to the previously described magnetization can be expressed by (cf. Bouligand et al. (2009); Maus et al. (1997))

$$\begin{aligned} \ln(\Phi(k_H)) = & A - 2k_H z_t - k_H \Delta z - \beta \ln(k_H) \\ & + \ln \left(\int_0^\infty (\cosh(k_H \Delta z) - \cos(k_z \Delta z)) \left(1 + \left(\frac{k_z}{k_H} \right)^2 \right)^{-1-\frac{\beta}{2}} dk_z \right), \end{aligned} \quad (2)$$

where $k_H = |\mathbf{k}_H|$ and $\mathbf{k}_H = (k_x, k_y)$ is the wavenumber in the horizontal plane; A is simply a constant determined by the proportionality constant C of the power spectrum Φ_M of the magnetization.

The computation of the radial power spectrum from data is typically done by a windowed Fourier transform of a magnetic anomaly map (the original magnetic data upward-continued to 5-km altitude relative to the WGS84 datum), where an adequately sized square window is moved across the study region (e.g., Bouligand et al. (2009); Li et al. (2017); Wang & Li (2015); Witter & Miller (2017)). Such windowing procedures may lead to ‘spectral leakage’ that particularly affects the low wavenumbers of the power spectrum. In order to reduce such effects, Gaudreau et al. (2019) have proposed a wavelet approach where they compute the wavelet transform

$$W_{a,\mathbf{b}}[f] = \int_{\mathbb{R}^2} f(\mathbf{r}) \psi_{a,\mathbf{b}}(\mathbf{r}) d\mathbf{r}, \quad (3)$$

of the magnetic anomaly map f at varying scales a (decreasing a indicate an increasing spatial localization of the wavelet $\psi_{a,\mathbf{b}}$). This does not require explicit windowing and all available data can be used for the computation of $W_{a,\mathbf{b}}[f]$. The parameter \mathbf{b} denotes the spatial shift of the wavelet and corresponds to the locations for which we want to evaluate the power spectrum (comparable to the center of the window if one were using a windowed Fourier transform). The scale parameter a of the wavelet transform can be related to a specific wavenumber k_H , which enables the use of wavelet transforms for the estimation of the radial power spectrum Φ , and which is indicated in more detail in Gaudreau et al. (2019); Kirby (2005). We will use their approach to obtain the radial power spectrum from the WDMAM2 magnetic anomaly map (cf. section

3.1 for the description of the used data) based on wavelet transforms. Once the power spectrum is computed from the available data, it can be compared to the theoretical expression in (2) in order to obtain information on the parameters A , z_t , β , and z_b , and the goodness of fit is calculated using the reduced chi-square statistic.

The inherent shortcomings of the power spectrum approach have been discussed extensively in some of the previously mentioned references on Curie depth estimation: the assumption of the magnetization being self-similar is contradictory to the expression via Fourier integrals (this can be ameliorated by conceiving it in terms of "bandlimited self-similarity"; Maus et al. (1997)); low wavenumber contributions of the power spectrum are difficult to compute reliably from magnetic anomaly data (cf. Bouligand et al. (2009) for an investigation in terms of the windowed Fourier transform; here, we ameliorate these problems by use of wavelet transforms as in Gaudreau et al. (2019)); the parameters A , z_t , β , z_b are strongly interrelated, e.g., an increase in β can be compensated by a decrease in z_b (cf. Bouligand et al. (2009) for a study on this; in section 4.1.1 we also briefly comment on this).

2.1.1 Bayesian Setup

In what follows, we describe the Bayesian framework that we use to obtain information on A , z_t , β , and z_b . We are interested in posterior distribution $P(\mathbf{m}|\mathbf{d})$ of the parameters $\mathbf{m} = (A, z_t, \beta, z_b)$, provided some input data \mathbf{d} (in our case, this will be the radial power spectrum $\mathbf{d} = (\Phi(k_H^1), \dots, \Phi(k_H^n))$ at various wave numbers k_H^1, \dots, k_H^n ; obtained via wavelet transforms of a magnetic anomaly map). Our later illustrations on the obtained Curie depth z_b (cf. figure 5) represent the mean of this posterior distribution, while the uncertainty is expressed in terms of the variance of the posterior. The classical Bayes formula for the posterior reads as follows:

$$P(\mathbf{m}|\mathbf{d}) \propto P(\mathbf{d}|\mathbf{m}) P(\mathbf{m}), \quad (4)$$

where $P(\mathbf{d}|\mathbf{m})$ denotes the likelihood and $P(\mathbf{m})$ the prior. The prior is chosen to be a uniform distribution, not preferring any particular value of the parameter set. However, for our Curie depth models we fix the depth to the top of the magnetization z_t (this is done by the sediment thickness provided by CRUST1.0, assuming that the magnetization of sediments is negligible; cf. section 3.3), and we also fix the fractal parameter β (but we run the computations for various fixed β in the range of 1.5 to 4.0, with grid step 0.5, values that have been considered reasonable by earlier geological studies). In other words, our prior only assumes a uniform distribution of the parameters $\mathbf{m} = (A, z_b)$. In section 4.1.1, we briefly illustrate the influence of considering β as an additional free parameter in the Bayesian setup. The likelihood is assumed to be a Gaussian distribution whose mean value $\mu_{\mathbf{m}}$ is provided by the theoretical power spectrum (2) and whose variance $\sigma_{\mathbf{d}}^2$ is computed from the input magnetic anomaly map. This leads to the following expression of the posterior distribution:

$$P(\mathbf{m}|\mathbf{d}) = C \exp \left(- \sum_{i=1}^n \frac{|\mu_{\mathbf{m}}^i - d_i|^2}{2 |\sigma_{\mathbf{d}}^i|^2} \right), \quad (5)$$

for some constant C . This distribution is then sampled via a Metropolis-Hasting algorithm in order to obtain the posterior mean and variance of the parameters \mathbf{m} , in particular of z_b (cf. Mather & Fulla (2019); Mather & Delhay (2019) whose code we will be using here).

2.2 Geothermal heat flow

To determine the heat flow distribution, we assume steady state conditions with no lateral variation in material properties and heat production (e.g., Afonso et al.

(2019)). Then, Fourier’s Law states:

$$K_1 \frac{\partial T(z)}{\partial z} = -q(z), \quad (6)$$

where T is the temperature, z is the depth, and K_1 and $q(z)$ are the thermal conductivity and heat flux, respectively. If initial conditions are provided by knowledge of z_b as the Curie depth, T_c as the Curie temperature ($\sim 580^\circ\text{C}$) and T_0 as the surface temperature, then the solution of the differential equation above leads to the following expression for the surface heat flow (e.g., Martos et al. (2017)):

$$q_s = \frac{K_1(T_c - T_0)}{z_b} + H_0 h_r - \frac{H_0 h_r^2}{z_b} \left(1 - e^{-\frac{z_b}{h_r}}\right), \quad (7)$$

where H_0 is the radiogenic heat production, and h_r is the scale depth at which H_0 decreased to $1/e$ of its surface value; assuming an exponential decrease of heat production with depth (e.g., Lachenbruch (1970)).

Later on, we refer to this setup as 1-D model or “constant conductivity model” because we assume K_1 to be constant within the entire crust and mantle. The corresponding surface heat flow models indicated in sections 4.2 and 5.1 are computed from (7), using the Curie depth z_b obtained in section 4.1 and fixing $H_0 = 2 \mu\text{W}/\text{m}^3$, $h_r = 10$. The outcome is typically indicated for various (but fixed) thermal conductivities K_1 (Martos et al., 2017). Furthermore, we provide some basic indicators of uncertainty for the heat flow: we compute q_s based on z_b as well as on $z_b \pm \sigma$ (where σ denotes the uncertainty of z_b as indicated in the results in section 4.1) and provide the maximum of the residuals between the three resulting outcomes as a measure of uncertainty for the surface heat flow q_s .

2.2.1 Varying thermal conductivities

In addition to the 1-D model from above, we consider a setup where thermal conductivities may vary. We allow different thermal conductivities K_1 and K_2 within the crust and the mantle, respectively. Furthermore, the heat flux is assumed to be purely vertical and each lithospheric column is in thermal equilibrium. Thus, within each column, K_1 and K_2 are constant, but the thermal conductivities are allowed to vary (laterally) among the different columns.

Given this setup, Fourier’s law (6) can be used to derive the temperature dependence with respect to depth (e.g., Lösing et al. (2020)), analogously to the 1-D case indicated above. Assuming that no heat is produced within the lithospheric mantle, the temperature in the lithospheric mantle at depth z is expressed as follows:

$$T(z) = T(M) + \frac{q_D}{K_2}(z - M), \quad (8)$$

where M is the Moho depth and q_D is the heat flux at the Moho boundary. Within the crust, the temperature can be expressed more generally in the form

$$T(z) = T_0 + \frac{q_s z - \bar{H}(z)}{K_1}, \quad (9)$$

where $\bar{H}(z) = \int_0^z H(s)ds$, and $H(z)$ is the total heat production. We assume that the heat production decays exponentially with depth, so that $H(z) = H_0 \exp(-z/h_r)$. In this case, (9) is just a rearranged version of (7). The heat flux $q(z)$ at any specific depth z within the crust is equal to the surface heat flux q_s minus the total heat production, so that we obtain the following simple relation between the surface heat flux q_s and the heat flux q_D at the Moho:

$$q_D = q_s - H(M). \quad (10)$$

Equations (8), (9), (10) allow to relate q_s , q_D , H_0 , K_1 , K_2 to the temperatures T_0 , T_c , T_{LAB} at the surface, at the Curie depth z_b , and at the Lithosphere-Asthenosphere boundary z_{LAB} , respectively.

A Bayesian framework almost identical to that in section 2.1.1 can then be used to invert the input $\mathbf{d} = (T_0, T_c, T_{LAB})$ for the parameters $\mathbf{m} = (q_D, H_0, K_1, K_2)$ within each lithospheric column (provided that we have knowledge of M , z_{LAB} , and z_b). Opposed to the setup of the 1-D model from before, the thermal conductivities K_1 , K_2 are not fixed anymore but will be inverted for jointly with the heat flux q_D at the Moho and the radiogenic heat production H_0 . For more details, we refer the reader to Löising et al. (2020), whose code we will be using here. The main quantity of interest to us is the posterior mean of q_D that allows to obtain the desired surface heat flow q_s via (10).

The input temperatures are set to the values $T_0 = 0^\circ\text{C}$, $T_c = 580^\circ\text{C}$, $T_{LAB} = 1315^\circ\text{C}$, as is also done in related works. The underlying Moho depths M and the Lithosphere-Asthenosphere boundary z_{LAB} stem from the models described in section 3.4, while we use our results from section 4.1 for the required Curie depths z_b . The uncertainties available for z_b are used in an identical way as in the 1-D model setup to provide basic indicators of uncertainty for the surface heat flow q_s . The results are illustrated in section 5.1 and we refer to this setup as “varying conductivity model”.

3 Data

In the following section we describe the datasets used in the study, and any necessary initial data preparation. We limit the model to the continental area, the overview of used data is provided in Table 1.

3.1 Magnetic Data

We used the magnetic data from the recently released World Digital Magnetic Anomaly Map 2.0 (WDMAM 2.0) (Lesur et al., 2016; Catalán et al., 2016). WDMAM 2.0 provides a 5km raster (grid) of magnetic anomalies, jointly compiled from marine cruises at sea level and airborne surveys at 5km height. All data are upward-continued to 5-km altitude relative to the WGS84 datum. WDMAM are continuously updated in the framework of an international scientific project, which runs under the auspices of International Association of Geomagnetism and Aeronomy (IAGA) and Commission for the Geological Map of the World (www.wdmam.org).

The African magnetic mapping project (Green et al., 1992) led to the SaNaBoZi aeromagnetic grid (Figure 2); the name stands for South Africa, Namibia, Botswana, and Zimbabwe (Stettler et al., 2000). The SaNaBoZi grid and more recently acquired grids over Zambia and Mozambique as well as marine data offshore of South Africa have been compiled and are part of the second version of the WDMAM (Lesur et al., 2016) used in this study (Figure 2).

Here, we will briefly summarize the regional-scale magnetic features in the study area. The Namaque-Natal domain is characterized by a remarkable, broadly spatially coincident, continental-scale magnetic anomaly, namely, the Beattie Magnetic Anomaly (BMA described by (Scheiber-Enslin et al., 2014; Cornell et al., 2011)) which extends from the western to the eastern coastal margins for more than 1100 km. To the North, the Kalahari magnetic lineament (Botswana Geological Survey Department et al., 1978) is characterized by short-wavelength magnetic anomalies which interpreted as the western boundary of the Kaapvaal Craton. This anomaly is one of the most dramatic features in the aeromagnetic image of southern Africa. Within the Kaapvaal Craton, long-wavelength magnetic anomalies are characterizing the Colesberg magnetic lineament. The boundary between the Kaapvaal Craton and

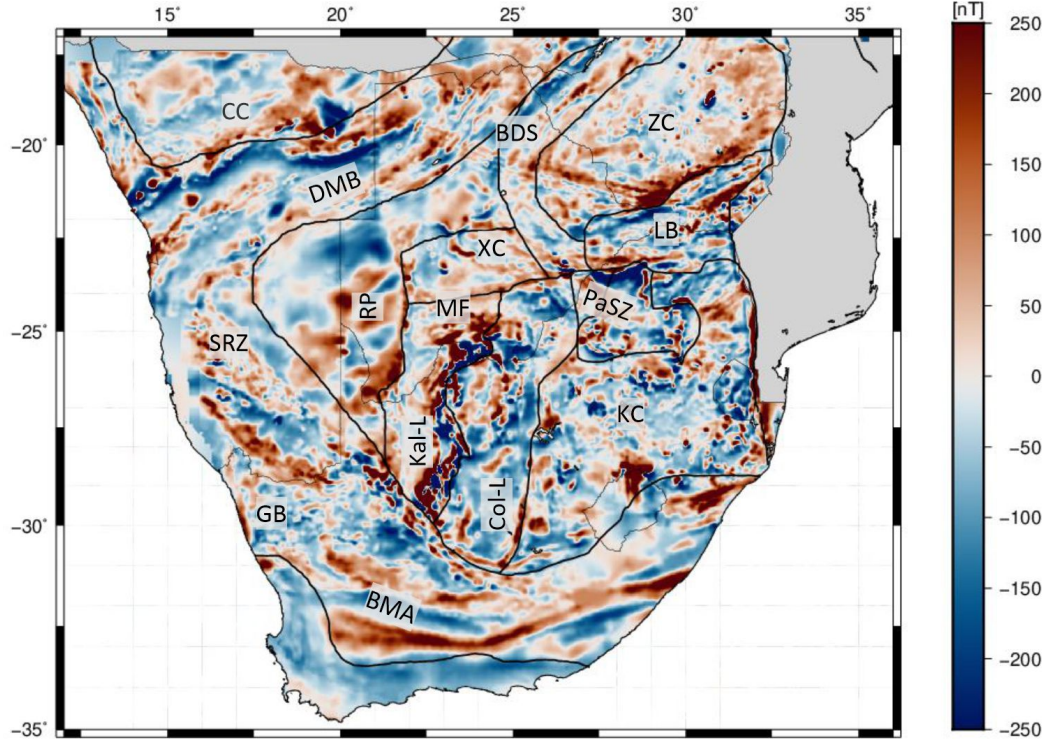


Figure 2. Total Magnetic Intensity (TMI) map of southern Africa from WDMAM2.0 (Lesur et al., 2016) with 2 arc-minute grid spacing (approximately 4 km). The original data are upward-continued to 5-km altitude relative to the WGS84 datum. Black lines represent the major tectonic provinces of southern Africa (de Wit et al., 1992). BMA = Beattie Magnetic Anomaly; BDS = Botswana Dyke System; CC = Congo Craton; Col-L = Colesberg Lineament; DMB = Damaran Mobile Belt; GB = Gariep Belt; KC = Kaapvaal Craton; LB = Limpopo Belt; MF = Molopo Farm; PaSZ = Palala Shear Zone; RP = Rehoboth Province; SRZ = Sinclair-Rehoboth Zone; ZC = Zimbabwe Craton.

the Limpopo Belt is characterized by a long-wavelength magnetic anomaly associated with the Palala shear zone (PaSZ). Moving to the North, the boundary between the Zimbabwe Craton and Limpopo Belt is relatively well defined from a clear change in the magnetic anomaly across the boundary. Moving towards the west, the magnetic anomalies along the Karoo basalts are shown in Botswana as well as the Botswana dyke swarm. In Namibia, long-wavelength, curvilinear magnetic anomalies are observed which associated with Sinclair-Rehoboth Zone (Van Schijndel et al., 2011). A weak imprint of the Beattie anomaly is visible even in the satellite lithospheric magnetic field model LCS-1 by Olsen et al. (2017) (Ebbing, Dilixiati, et al., 2021) (see Figure S1 of supplementary material), which confirms its regional significance.

3.2 Heat Flow Data

The compilation of surface heat flow data used in this work (Figure 3-a) comes from different sources (e.g., Pollack et al. (1993)). Lucazeau (2019) compile all available data in the New Global Heat Flow database (NGHF), which is an extended compilation of earlier heat flow catalogs, associated with meta data attributes with links to original studies. Measurements are, however, irregular in distribution and of varying quality. The quality of heat flow measurements are rated in NGHF. The rating category for each measurement is based on e.g. the variation of heat flow in the borehole where the measurement is performed. Old and questionable measurements are generally assigned a lower rating. According to the NGHF database, most of heat flow data used here have an uncertainty between 10 and 20 mW/m² (Lucazeau, 2019) (see Figure S2 of supplementary material). In general, the Kaapvaal and Zimbabwe Cratons have a relatively low heat flow ($\approx 40\text{--}50$ mW/m²); these values increase to ≈ 60 mW/m² at the boundary between the Craton and the surrounding Proterozoic and Pan-African mobile belts. Mobile belts surrounding the Kaapvaal Craton exhibit the highest heat flow signatures in South Africa (≈ 70 mW/m²), which may be linked to underlying geological, tectonic and crustal compositional controls, particularly related to the heat production of radiogenic material.

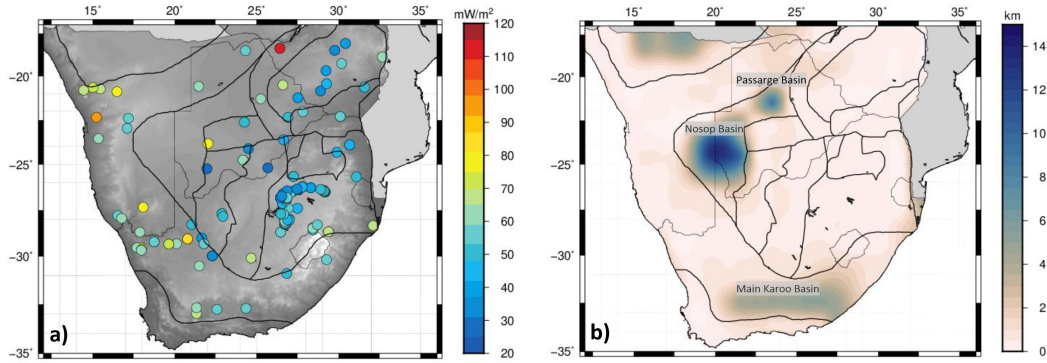


Figure 3. (a) Distribution of heat flow measurements within the study area from the global database (Lucazeau, 2019). The associated uncertainty of measured heat flow is shown in Figure S2. (b) Sediment thickness map of southern Africa extract from global sediment thickness map (Laske et al., 2013) used to constrain the depth of the upper boundary of magnetized layer (z_t) and fixed prior to the inversion. Major sedimentary basins are presented: Main Karoo Basin (Johnson et al., 1997); Nosop Basin (Wright & Hall, 1990); Passarge Bain (Key & Ayres, 2000a).

3.3 Sediment Thickness

The sedimentary data are extracted from the sediment layers of CRUST1.0 (Laske et al., 2013), defined on a $1^\circ \times 1^\circ$ grid, which we project and interpolate onto a rectangular grid with a sampling interval of 4 km to be compatible with the magnetic data resolution. The sediment thickness map in Figure 3-b is used to constrain the depth to the top of the magnetized layer (z_t), since sedimentary rocks are expected to be only weakly (para)magnetic (Ellwood et al., 2000) and their overall contribution is considered negligible.

3.4 Crustal and Lithospheric Thickness

For the purpose of comparing the bottom of the magnetized layer with the crustal thickness in the study area and to constrain the heat flow calculations from Curie depth, we estimate the Moho depth by inverting the satellite gravity gradients using the seismically constrained non-linear inversion scheme of Uieda & Barbosa (2017) (Figure 4-a). Since large contributions of the heat flow comes from radioactive decay of elements within enriched crust (Hasterok & Chapman, 2011), considering the crustal thickness in our modelling process can therefore substantially improve heat flow maps. The lithospheric thickness model (Figure 4-b) is derived from the global reference model of the lithosphere (Afonso et al., 2019) which is estimated from the joint inversion of satellite-derived gravity gradients, geoid height, and absolute elevation complemented with seismic, thermal and petrological information.

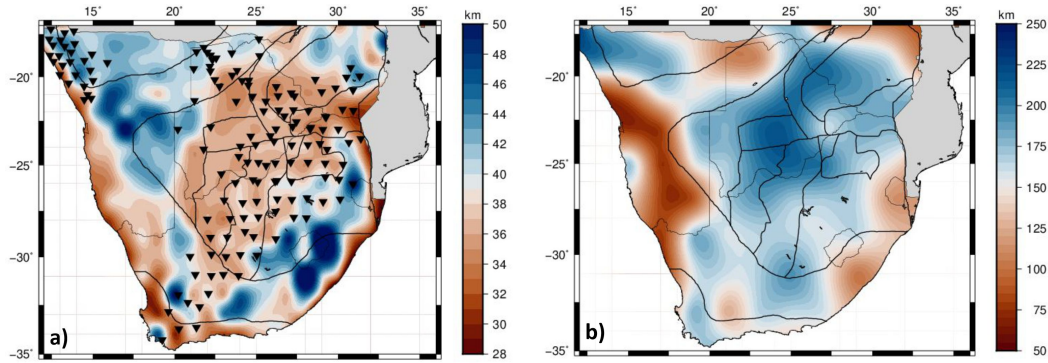


Figure 4. (a) Moho depth of southern Africa from the seismically constrained gravity inversion, the black circles represents the location of seismic stations used to constrain the gravity inversion for Moho depth (b) Lithosphere-Asthenosphere boundary (LAB) depth derived from LithoRef18, the global reference model of the lithosphere (Afonso et al., 2019).

4 Results

We present Curie depth maps and consequently heat flow maps, together with maps of uncertainty.

4.1 Curie Depth Estimates

The presented results in this section are shown as maps of the depths to the bottom of the magnetic layer (z_b), which will be interpreted as Curie depth, together with the estimated uncertainties. The outcome is based on the procedure described in Section 2.1 and the data from Sections 3.

351

Table 1. Summary of datasets and parameters used in the modelling process.

Data	Reference
Geophysical	
Magnetic data	WDMAM2 (Lesur et al., 2016)
Heat flow	NGHF (Lucazeau, 2019; Pollack et al., 1993)
Geometrical	
Sediment thickness	CRUST1.0 model (Laske et al., 2013)
Moho depth	Gravity inversion(Uieda & Barbosa, 2017) with seismic constraints (Fadel et al., 2020; Youssef et al., 2013)
Base lithosphere	LithoRef18 (Afonso et al., 2019)

360

361

362

363

364

365

366

367

368

369

370

371

As mentioned earlier, estimating all quantities z_b , z_t , and β simultaneously may lead to ambiguous values for z_b (illustrated, e.g., in Bouligand et al. (2009)). Therefore, in this study, we fix β to a constant value for the entire study area. However, multiple maps of z_b created using different (but fixed) β ranging from 2.0 to 3.0, which are typical values estimated in crustal rocks (Maus et al., 1997; Maus & Dimri, 1996; Pilkington & Todoeschuck, 1993) are shown in Figure 5. The top of the magnetic layer (z_t) is fixed as well and not changed throughout the study. It is constrained by the sedimentary thickness model shown in Figure 3-b, since this layer is most likely weakly magnetic and is assumed to not contribute to the magnetic anomalies. Yet, to provide at least a brief illustration of the influence of fixing these parameters in our setup, we use subsection 4.1.1 to indicate the joint probabilities of the inversion at selected locations when inverting for all three parameters simultaneously.

372

373

374

375

376

377

378

379

380

381

382

383

384

Figure 5 shows the inversion results with fixed parameters as mentioned above. One can observe that an increase of β leads to a substantial decrease of the estimated z_b . This has also been illustrated in the synthetic examples in Section 3.3 of Bouligand et al. (2009). As the β parameter increases from 2.0 to 3.0, the mean z_b value in the Kaapvaal Craton decreases from 50 to 15 km. The mean z_b within the Kheis Belt ranges from 25 to 5 km, and in the Zimbabwe Craton, the mean z_b ranges from 50 to 25 km. Along Damara Mobile Belt, the mean z_b is ranging from 15 to 5 km at the North Botswana, with β increasing from 2.5 to 3.0. The mean z_b along Namagua-Natal Belt, ranges from 50 to 30 km. However, Figure 5-a also indicates that the patterns of the estimated Curie depth are robust with respect to β (i.e., regions that reveal a shallow Curie depth compared to deeper surrounding regions remain shallow in this relative sense across the whole range of tested values of β) and, therefore, can provide some reliable geophysical information about the observed Curie depth patterns.

394

395

396

397

398

399

400

401

402

403

404

405

406

The depth to the bottom of magnetisation varies across southern Africa from 20 to 50 km beneath Kaapvaal and Zimbabwe Craton, with uncertainties between 3 and 12 km, respectively. There is some exception along western part of Kaapvaal Craton which have much shallower depth to the bottom of magnetisation than other Archean Cratons despite the low surface heat flow values. This result may be explained by the fact that we may have modelled only the depth extent of magnetic minerals rather than the depth at which they have reached their Curie points. Furthermore, the very strong magnetic response from Ventersdorp magmatic intrusion (Neoproterozoic age) may be masking a more subtle signal of the deepest magnetic sources, which may well be less magnetic than this magmatic intrusion. The eastern margin of Kaapvaal Craton is modelled with shallow Curie depth along all the different β . This is probably due to the presence of Karoo lavas along the boundary between Kaapvaal Craton and Mozambique Mobile Belt. The western margin of the Kaapvaal Craton is modelled

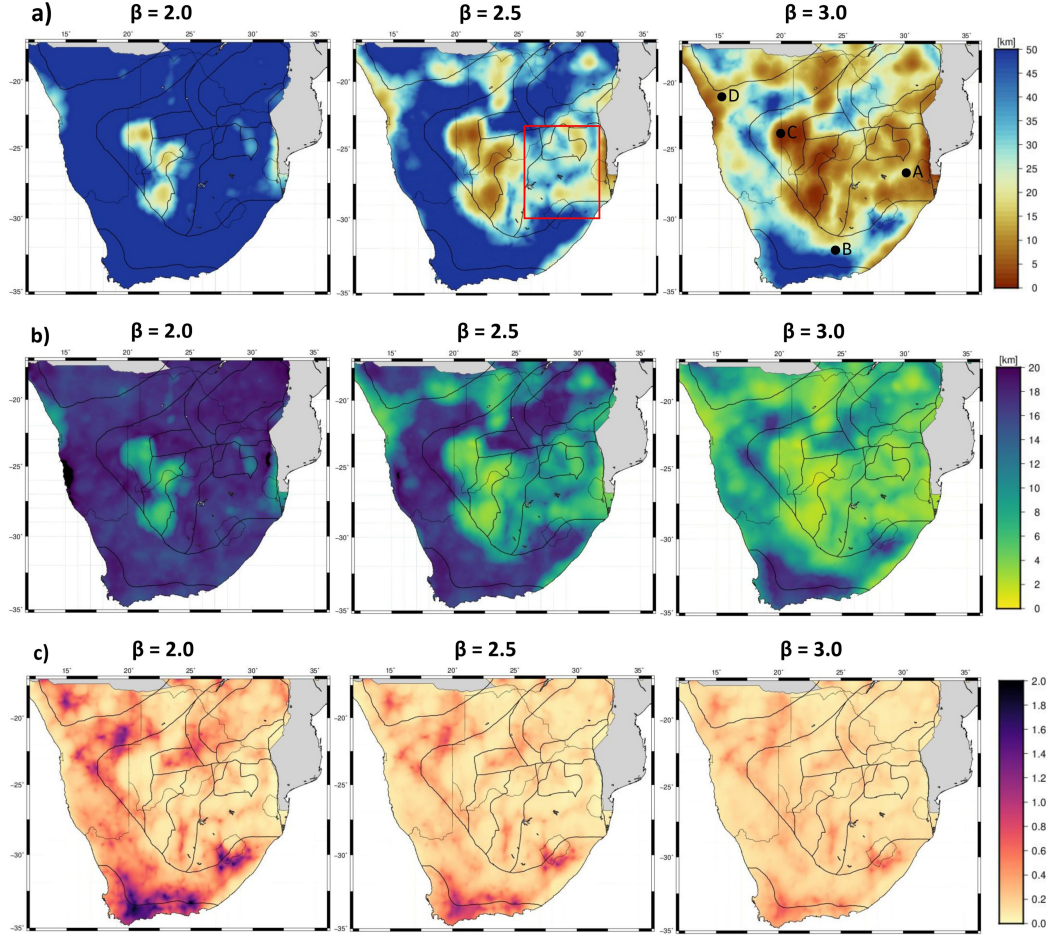


Figure 5. (a) Maps show the depth to the bottom of magnetic sources (z_b) based on the aeromagnetic data in southern Africa when depth to the top of magnetic sources (z_t) is set to the sediment thickness from Figure 3-b and for various β (assuming constant β values throughout the study area), illustrating the inverse relationship between the fractal exponent β and z_b . All maps display similar long-wavelength features that are independent of the values of β . The red box outlines the z_b along Kaapvaal region. The locations marked by the letters A,B,C, and D correspond to the maps in Figure 6, and Figures S3 : S5. (b) The 3σ uncertainty of the mean z_b in southern Africa. (c) Maps of the reduced chi-square statistic illustrating the fit between the calculated and the theoretical power spectra.

by shallow Curie depth which is related to reactivation of the Kheis province during Kibaran orogeny (Thomas et al., 1993). The Kheis Belt consists of basalts and clastic sediments located between the Kaapvaal Craton to the east and the Rehoboth terrane to the west. The Kheis Belt form a distinct highly magnetic feature that extends northwards to the Okwa Block (Hutchins & Reeves, 1980). Toward the Capo Fold Belt, the depth to the bottom of magnetization using different β values is very deep and not logic. But this is also the area with the most significant uncertainty and the highest reduced chi-square. Our Curie depth map with $\beta = 3.0$ (cf. Figure 5-a) is, for the most part, concordant with the global reference model of (Li et al., 2017) and follows a similar pattern of variation as we observe along Kaapvaal Craton.

The uncertainty and reduced chi-square of the fitted parameters associated with the estimated Curie depth are shown in Figures 5-b and c, respectively. Generally, the shallow Curie depths are associated with low uncertainties, and deeper Curie depths have a significantly higher uncertainty. This may be due to difficulties in the estimation of the small wave number portion of the radial power spectrum. Within each map in Figure 5-b, the estimated z_b uncertainty is high where the z_b values are deeper than 50 km, and decreases with increasing β . The reduced chi-square value in the Kheis Belt and Kaapvaal Craton remains relatively constant in the different inversions, but decreases with increasing β in Damara Mobile Belt and Cape Fold Belt (Figure 5-c). For all β values, the reduced chi-square is highest where is deeper than 50 km.

4.1.1 Multiparameter Study for Selected Locations

In this section we briefly want to indicate the influence of fixing the parameter β for selected locations. Namely, we allow all parameters $\mathbf{m} = (A, \beta, z_b)$ to vary and illustrate their marginal and joint posterior probabilities based on the methodology described in Section 2.1 (the top depth z_t remains fixed). The four specific locations for this study are those that are indicated by the letters A, B, C, and D in Figure 5-a (representing different tectonic domains within the study area).

In each case, the first step is to estimate the three parameters z_b , β , and A simultaneously (Figure 6-a). Subsequently, β is fixed to the mean obtained in this first step and the inversion is done only for the two remaining parameters z_b and A (Figure 6-b), (see section 4.1 for more details). For the grid cell (A) in the Kaapvaal Craton, the results obtained from the joint inversion of all three parameters give a z_b of 26.4 km and an uncertainty of 13.2 km. The mean of β is 3.0 with an uncertainty of 0.4. Keeping β fixed and running the inversion again, the uncertainty of z_b reduces to 10.4 km with a mean of 29.3 km, analogous to what has been obtained in Figure 5-b. The result for the other three test sites (B, C, and D) are shown in Figures S3:S5 in the supplementary material. The key outcome here is that the mean β obtained during the simultaneous inversion for all three parameters z_b , β , and A varies across all four tested tectonic domains. Nonetheless, the obtained β for any of these domains corresponds to one of the β for which the Curie depth has been computed and indicated over entire southern Africa in Figure 5-a. This should be kept in mind when interpreting inversion results for z_b with fixed β , and the appropriate map should be chosen.

4.2 Heat Flow Estimates

In this study, we assume a Curie temperature of the crustal rocks in southern Africa of around 580°C, which corresponds to the Curie temperature of magnetite (Dunlop & Özdemir, 2001). The quantitative comparison between Curie depth and heat flow measurements was performed to validate the results of Curie depth and evaluate the method to determine it from magnetic data.

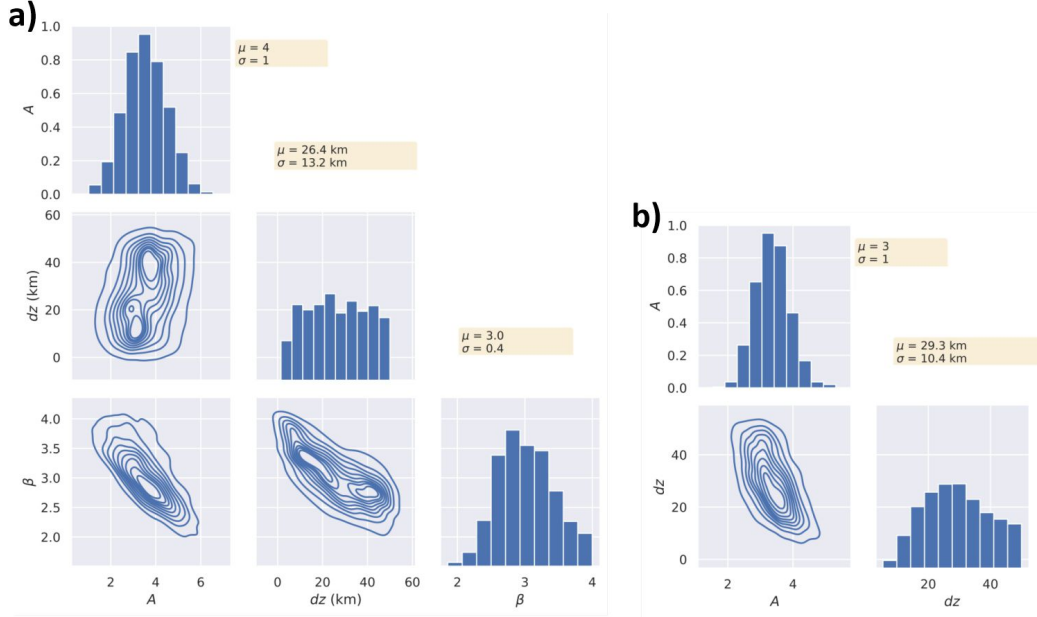


Figure 6. Statistical distribution of model parameters from at location A of Figure 5-a: marginalized and joint posterior distribution from the simultaneous inversion for the parameters z_b , β , and A (a) and for the simultaneous inversion for z_b and A , with fixed $\beta = 3.0$ (b). Statistical information on each z_b , β , A is provided in the orange boxes; μ is the mean value, σ is the standard deviation. Note that the parameter dz in the above plots indicates Δz in our notation, so that $z_b = z_t + dz$.

The distribution of heat flow measurements is shown in Figure 3-a. The heat flow measurements are relatively dense in Kaapvaal and Zimbabwe cratons, with values ranging from ~ 40 to ~ 60 mW/m², and along mobile belts ranging from ~ 55 to ~ 80 mW/m². On the other hand, the rest of the study area suffers from highly scattered and sparse distributions of heat flow measurements. The calculated heat flow values q_s from the 1-D model in section 2.2, based on equation (7) with $\beta = 2.5$, are plotted versus Curie Depth for different thermal conductivities K_1 (cf. Figure 7). We also included measured heat flow values from the global database Lucazeau (2019), plotted against the estimated Curie depths from section 4.1 at the measurement locations. Obviously this comparison has a significant degree of variance. Variances in the assumed parameters of the Curie depth modelling procedure (as indicated in Figure 5-b), uncertainties of the heat flow measurements, and uncertainties like lithologically bounded vs. thermally controlled magnetisation depths all add to the observed scatter of the fit. Unlike the first two points, the uncertainty due the lack of precise lithological bounds cannot be quantified by any of the existing methods. This is why we discuss in Section 5 the outcome of the Curie depth estimation and the heat flow estimation jointly with the geological situation in southern Africa. Figure 7 shows that in particular the shallow Curie depth reveal a large mismatch with the measured heat flow values, implying that these shallow depths might not represent the maximum depth of magnetic layer but correlate with the overprinted magmatic activities. Locally, however, the correlation can be quite good. Figure 8 shows an analogous scatter plot, but the z_b results are restricted to the Kaapvaal Craton, since it has dense heat flow measurements for better comparison.

As shown in our previous results, larger β than the correct value can be compensated by shallower z_b . Consequently, higher estimated heat flow are not necessarily related with the actual thermal state of the study area. Calibration of the results using some actual thermal gradient measurement could help to validate the heat flow results in the future.

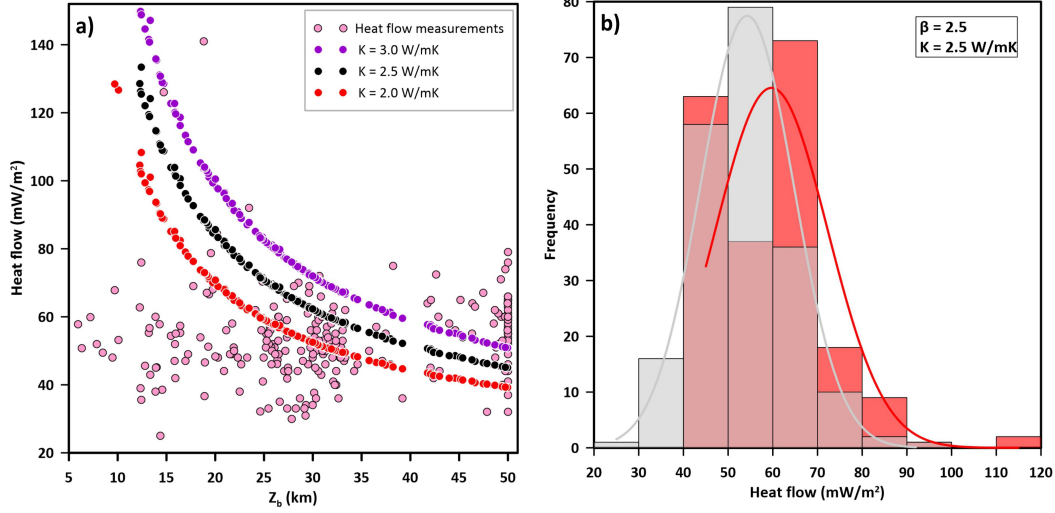


Figure 7. (a) Heat flow as a function of z_b . The curves plotted are the theoretical heat flow curves for different thermal conductivity 2.0 (red), 2.5 (black), 3.0 (purple). The scattered dots (light pink) represent the measured heat flow from Lucazeau (2019). (b) Frequency of estimated heat flow values (in gray) and of the measured heat flow values (in red).

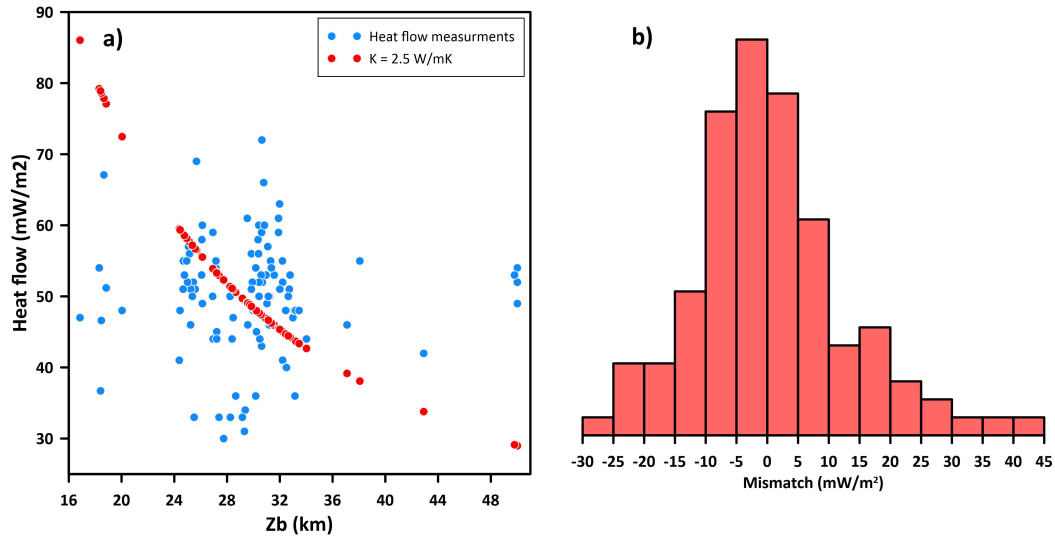


Figure 8. (a) Heat flow as a function of z_b . Same as in Figure 7, but restricted to the Kaavaal Craton. (b) Frequency of mismatch between the estimated and the measured heat flow.

5 Discussion

In this section, we first discuss the correlation between the mapped Curie depth and heat flow measurements (section 5.1), followed by discussing the benefits of varying the thermal parameters in modelling heat flow, we then note the limitations associated with the used methodology.

The relationships of our results to compilations of thermal estimates for the southern Africa highlight both areas where our depth to the bottom of magnetisation matches the expectations of Curie depth and areas where it does not. Such differences may indicate areas where our understanding of the thermal regime is incomplete, or could arise from differences in geology resulting from processes such as major tectonic events changing magnetic mineralogy. Comparing the estimated Curie depths with the magnetic data shows the following: the shallow z_b areas generally correspond to the short-wavelength dominated anomalies, such as in the magnetic signature of Kheis Belt and the Kalahari magnetic lineament (Figure 2); (Botswana Geological Survey Department et al., 1978). On the other hand, areas mapped with deep z_b generally correspond with the areas dominated by long-wavelength anomalies, such as the Beattie continental scale Magnetic Anomaly (BMA; (Scheiber-Enslin et al., 2014; Cornell et al., 2011)). Along the Okavango Rift Zone in the north-western part of Botswana, z_b is shallow ranging from 8-15 km which is coincident with the thermal perturbation of Okavango Rift (Leseane et al., 2015) and crustal thinning (Fadel et al., 2020). The first obvious observation was that the very shallow Curie depth in the middle of Botswana fell into the part of the sedimentary basins (Passarge and Nosop Basin) which are intruded by Xade complex and Okwa block (cf. Figure 1). Along the Molopo Farm ultra basic intrusion (Key & Ayres, 2000b), the Curie depth is shallow ranging from 15 - 20 km with β value 2.5. Toward eastern part of Botswana, the Curie depth is deep, which coincide with the Zimbabwe Craton and the old belts in this area. In South Africa, the Kaapvaal Craton and Venterschorp group magamtic intrusion are very visible in the magnetic anomaly map (cf. Figure 2), and this is reflected in the z_b maps (cf. Figure 5-a). Along Venterschorp group magamtic intrusion, the z_b values that are distinctly shallower than the rest of the southern Africa: when β is set to 3.0, the average z_b is ranging from 0-5 km. In contrast with Kaapvaal Craton: when β is set to 2.5, the average z_b is 30 km. Along Kalahari magnetic lineament, similar long-wavelength features for all values of β are shown, indicating that these patterns are robust and have geophysical significance. One could interpret the shallow z_b along Kalahari magnetic lineament as a lithological contact that represents the base of the magnetized crust, and that is shallower than the actual Curie depth (Blakely, 1988); however, there is no magmatic activity recorded along this area. A more reasonable explanation is that there is a strong change in lithology and geological history resulting in a different β value for the Kaapvaal Craton, and this is consistent with the heat flow modelling (cf. figure 9-a). Recently (Gard & Hasterok, 2021) have determined the Curie depth globally using satellite magnetic model LCS-1 (Olsen et al., 2017) from spherical harmonic degree 16 to 100 which is corresponding to wavelength of ~ 400 km using the equivalent source magnetic dipole method. They obtain deeper z_b along the Kheis Belt and the Kalahari magnetic lineament, due to the very long wavelengths dominating the used magnetic data which do not reflect the shorter wavelengths associated with the remarkable magnetic signature of the Kheis Belt (cf. Figure 9-b). Perhaps the most striking feature of the z_b maps in Figure 5 is the sharp transition between shallow (~ 20 km) and erroneous deep (> 50 km) z_b values which coincides with the thrust Fault separating between Namaqua-Natal Belt and Cape Fold Belt. Recent S-wave tomography and body wave tomography have demonstrated that this thrust faults is a crustal-scale structural feature that defines a major change in the geology (White-Gaynor et al., 2020; Celli et al., 2020). At all β values, the Cape Fold Belt shows high reduced chi-square values and high uncertainties, therefore indicating that the estimated Curie depth in this region cannot be obtained reliably.

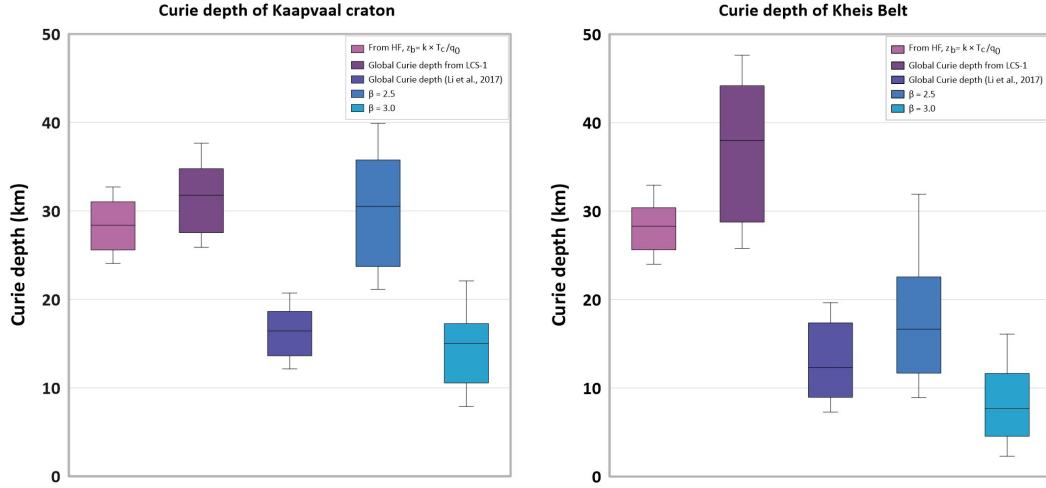


Figure 9. Comparison of estimated Curie depth along (a) Kaapvaal Craton; (b) Kheis Belt from our model using two different β values; global curie depth model (Li et al., 2017); from heat flow measurements, and from global curie depth model by utilising the equivalent source magnetic dipole (Gard & Hasterok, 2021)

5.1 Correlation Between Curie Depth and Heat Flow Measurements

Previous studies have showed that the Curie depths are inversely correlated to the heat flow (Li et al., 2017). We found in (Figure 7) that measured heat flow and the Curie depths estimates seem to be very poorly correlated and in most cases do not match the predictions of the 1-D thermal conductivity model from section 2.2. Locally, however, the situation can be better (e.g., for the Kapvaal Craton as indicated in Figure 8). In the following two subsections, we discuss the 1-D model as well as the model with varying thermal conductivities in some more detail.

5.1.1 Modelled heat flow from constant thermal conductivities

Figure 10 shows a comparison between heat flow estimated from Curie depth with constant thermal conductivity and heat flow measurements from the most recent compilation Lucazeau (2019).

The estimated heat flow calculated from the global Curie depth model of Li et al. (2017) in the southern Africa displays higher heat flow than our estimates for most study areas (cf. Figure S6). In the Kapvaal Craton, e.g., they suggest an area of high heat flow. The heat flow estimates based on our Curie depth model (with 2 and 2.5 β values) (Figure 10-a,b) suggests a zone of relatively low heat flow, in better agreement with the available measurements. This suggests that in spite of the limitations of the method used to calculate the depth to the Curie isotherm, it could be used to provide a lower thermal boundary condition for heat-flow calculations.

On the other hand, areas with short-wavelength features – that significantly influence the heat flow field – cannot be resolved adequately. For instance, the Kalahari magnetic lineament at the western part of Kaapvaal Craton is modelled with very high heat flow values and shows large discrepancies to the measured low heat flow values, indicating that the estimated shallow Curie isotherm in this area might have a structural rather than a thermal origin.

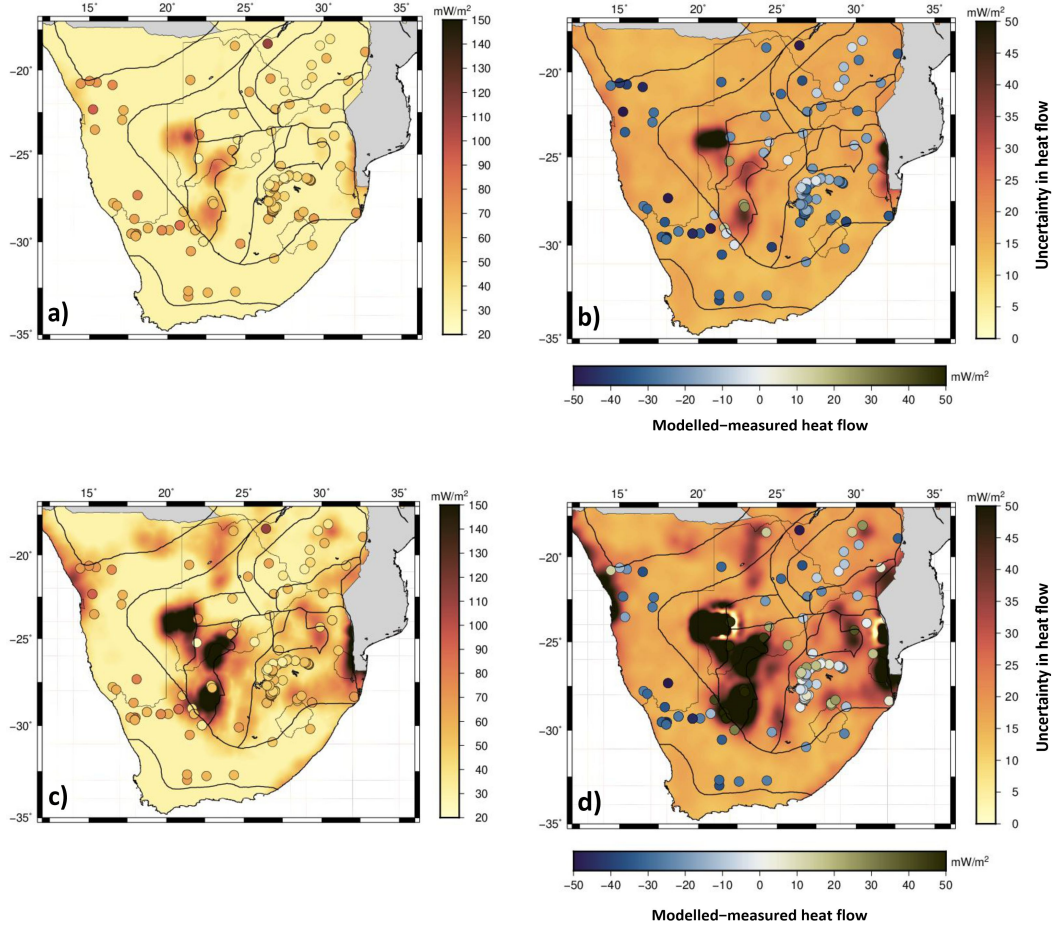


Figure 10. Modelled heat flow using the 1-D heat conductive model with laterally constant thermal conductivity ($k = 2.5 \text{ W/mK}$) at the Curie depth estimated when (a) $\beta = 2.0$; (c) $\beta = 2.5$ overlain with the locations of the measured heat flow data. Uncertainty of heat flow determined from an ensemble of model simulations for the estimated Curie depth with $\beta = 2.0$ (b); with $\beta = 2.5$ (d) overlain with the locations of the difference between modelled and measured heat flow.

5.1.2 Modelled heat flow from varying thermal conductivities

In Figure 11 we indicate the outcome for the heat flow similar to Figure 10, but this time allowing varying conductivities within the Bayesian framework described in section 2.2.1 and Lösing et al. (2020).

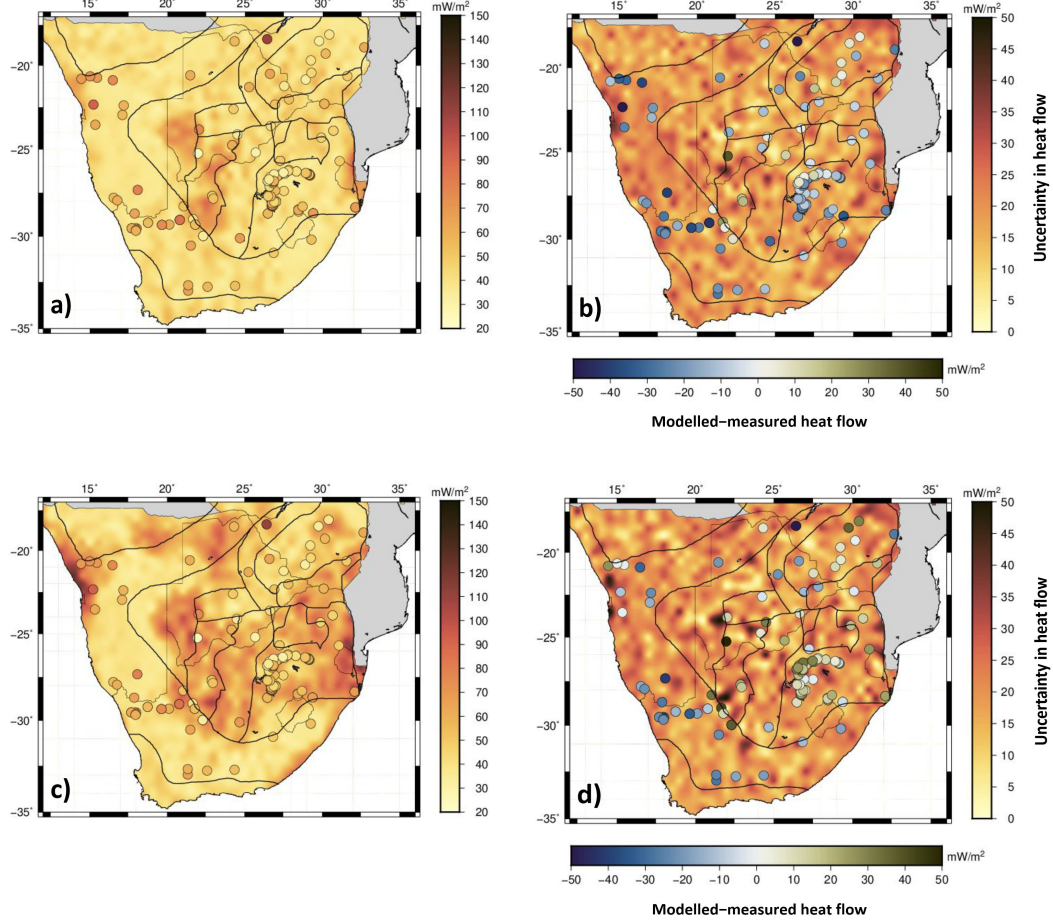


Figure 11. Modelled heat flow in Southern Africa and its uncertainty. Heat flow distribution calculated from the setup in section 2.2.1 and Lösing et al. (2020) for the estimated Curie depth with $\beta = 2.0$ (a); with $\beta = 2.5$ (c). Uncertainty of heat flow determined from an ensemble of model simulations for the estimated Curie depth with $\beta = 2.0$ (b); with $\beta = 2.5$ (d) overlain with the locations of the difference between modelled and measured heat flow.

The mantle heat flux q_D (Figure S7) correlates strongly with the LAB depths. A similar pattern is observed for crustal heat production, which correlates with the Moho depth. In addition, there is a strong linear relation between heat production and heat flow, which has been demonstrated empirically in Roy et al. (1968) (for more details, see Figure S7).

Both, heat production and the calculated heat flow (Figure S7) strongly resemble the Curie isotherm (Figure 5-a). In areas of deeper Curie depths down to 40 km the heat flow is between 30 and 40 mW/m² with low heat production below 1.0 $\mu\text{W}/\text{m}^2$. In shallower Curie depth regions between 15 and 20 km, the heat flow reaches up to 100 mW/m² and exhibits higher heat production rates around 2.5 $\mu\text{W}/\text{m}^2$.

Two Curie depth models (with different β values 2.0 and 2.5) have been tested (Figure 11), with use of a fixed Moho depth and LAB (Figure 4). The Moho depth has an influence on the crustal heat production, i.e., a thin crust is compensated with higher rates of heat production. It is noticeable that the heat flow is most affected by changing the Curie depth and the spatial distribution of the heat flow is mirrored by the Curie isotherm. For example in Cap Fold Belt we observe areas of low heat flow, correlating with unrealistic deep Curie depths. These areas also correspond to higher uncertainties of curie depth estimation and high chi-square values. The remaining inverted thermal parameters (Figure S7) do not show significant differences from $\beta=2.0$. The spatial distribution of the modelled heat flow in Figure 11 shows similar patterns in most places as the modeled heat flow presented in Figure 10, although the latter used laterally constant heat production rates with a surface value of $H_0 = 2.5 \mu\text{W}/\text{m}^2$ and constant crustal thermal conductivity of $2.5 \text{ W}/\text{mK}$. The two models are greatly comparable and the average residual heat flow between the inversion with variable heat production (Figure 11) and the laterally constant heat production results (Figure 10) is approximately $\pm 4 \text{ mW}/\text{m}^2$, indicating the strong influence of the Curie isotherm for the heat flow calculation. Along the Kalahari magnetic lineament, the inversion results in Figure 11 show lower heat flow values, resulting from using laterally variable thermal conductivity and heat production values.

Both modelled heat flow using the two different approaches (laterally constant or variable heat production) show some degree of agreement compared to the measured heat flow values, however, with large discrepancies in most places. The possible origins of that are shown below:

- The shallow, spatially large magmatic provinces that run parallel to the Kalahari magnetic lineament can cause Curie depths to be underestimated;
- magmatic rocks with a large magnetic field may intrude and cover a less magnetic metamorphic basement and extremely weakly magnetic basin sediments;
- instead of giving a depth to the bottom of the magnetic source, the spectrum approach can give a depth to the bottom of magnetization that corresponds to the base of the dominant unit, i.e. the volcanic rocks, and in this case the thickness of superficial rocks might then be estimated;
- notwithstanding the possibility of other geological restrictions, the assumption that the depth to the bottom of the magnetic source is temperature-controlled (i.e. it reflects the Curie isotherm).

5.2 Comparison of Crustal Thickness With Curie Depths

Most early studies considered the mantle to be nonmagnetic (Wasilewski et al., 1979; Wasilewski & Mayhew, 1992); however, recent studies (Ferré et al., 2014) argue for the occurrence of a magnetized upper mantle in certain geological contexts. Here we make the approximation that, if the uppermost mantle is magnetized, its susceptibility is likely much lower than that for crustal rocks, and therefore, we consider a maximum Curie depth of 50 km.

A comparison between the crustal thickness and Curie depth is presented in Figure 12. Negative values represent Curie depth values deeper than the Moho and positive values represent areas where the Curie depth is shallower than the Moho. Figure 12-a shows negative values in large areas, meaning the calculated Curie depth is deeper than the gravity inverted Moho depth (cf. Figure 4) for large areas if $\beta = 2.0$. If $\beta = 2.5$, as indicated in Figure 12-b, the calculated Curie depth is shallower than Moho depth for a fairly large portion of the investigated area.

However, whilst in general the Earth's mantle does not contribute to the magnetic signal (due to its weak magnetization and high temperature conditions), in some

cases the Curie depth may indeed lie within the mantle. This occurs where metallic magnetic phases in the mantle beneath old and tectonically stable crust (Cratons; Ferré et al. (2014) or subduction regions; Blakely et al. (2005)) contribute to mantle magnetization. In these settings the crust–mantle boundary should not be considered an absolute magnetic boundary (Ferré et al., 2014). This implies that if in a given region the Moho depths are shallower than the deepest magnetic layer, a magnetic mantle at temperatures below the Curie temperature may be considered. However, even in these cases the upper mantle susceptibility will be more than 1–2 orders of magnitude smaller than the overlying crust. This is not considered in current spectral methods for Curie depth estimation and any Curie depths below Moho depths are ruled out or interpreted as a structural rather than a thermal source.

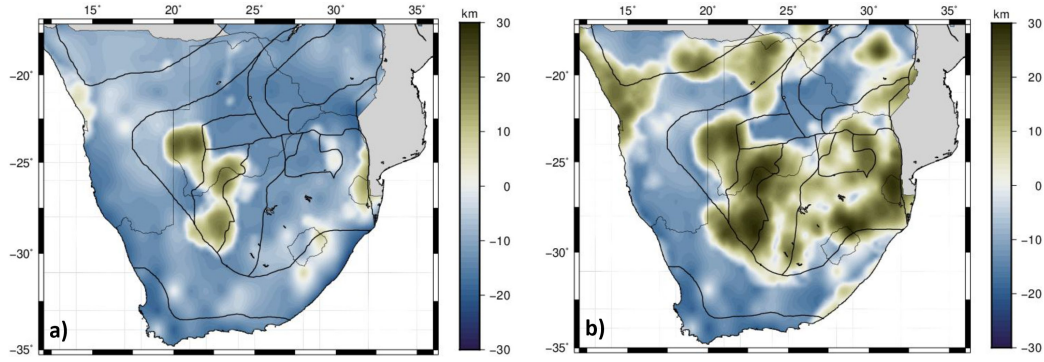


Figure 12. Comparison of Curie depth and depth of the crust–mantle boundary (the Moho depth) derived from gravity inversion with seismic constraints, (a) with $\beta = 2.0$ and (b) with $\beta = 2.5$. Negative values show areas where the estimated Curie depth is deeper than the estimated Moho depth, and positive values are where the Curie depth is shallower than the Moho depth.

Figure 12-a shows that the magnetic bottom extends deeper than the Moho discontinuity, reaching the upper mantle and indicating that the Curie depth results with $\beta = 2.0$ is not realistic in most places along the study area. Figure 12-b shows in large area that the Curie depth is shallower than the Moho depth and it correlates well with the uncertainty map for Curie depths, assuming $\beta = 2.5$. The areas where the Curie depth is deeper than the Moho are associated with high uncertainties in the Curie depth (cf. Figure 5-b).

6 Conclusions

The study estimates the Curie depth z_b over southern Africa using wavelet transforms of magnetic data in combination with a Bayesian setup. The sedimentary layer thickness used to constrain z_t remains fixed in the inversion and we test various values for the fractal parameter β , which very roughly characterizes the structure of the underlying crustal magnetization. The uncertainty in Curie depth estimation is provided along the entire study area, using probabilistic Bayesian inference method and to show the statistical distribution of the model parameters.

We observe correlations of shallow z_b with the distribution of magmatic rocks at the western boundary of Kaapvaal Craton, which is consistent among different β values, indicating that the modelled z_b might correspond to the base of highly magnetized young volcanic rocks instated of Curie temperature isotherm.

We further used the estimated Curie depth to model surface heat flow, in a setup with assumed constant thermal conductivity as well as with varying thermal conductivities. The modelled heat flow matches heat flow data to a reasonable degree of uncertainty, except in regions where magmatic intrusions are presented (e.g., Kalahari magnetic lineaments). The spectral analysis of magnetic anomaly data may be better suitable to hotter settings, where shallow Curie depth estimates are more robust, and in the oceans, where magnetization is likely to be uniform.

Our results raise a major future directions of improvement. It may be possible to use additional constraints on z_b by considering available heat flow measurements into the inversion process, which impose physical bounds on the predicted Curie depth via thermal models.

Acknowledgments

MS and CG have been partially funded by BMWi (Bundesministerium für Wirtschaft und Energie) within the joint project 'SYSEXPL – Systematische Exploration', grant ref. 03EE4002B. IF have been funded by Nederlandse Organisatie voor Wetenschappelijk Onderzoek (NWO), grant ALWGO.2019.054. All grid files and maps were created using Generic Mapping Tools (GMT) version 5 (Wessel et al., 2013). The scientific color map was used in this study to prevent visual distortion of the data and exclusion of readers with color vision deficiencies (Crameri et al., 2020). The aeromagnetic data is available at (<http://wdmam.org/>) (Lesur et al., 2016). The sediment thickness model is available at (<http://igppweb.ucsd.edu/~gabi/crust1.htm>) (Laske et al., 2013). The heat flow data are available at (<http://www.heatflow.org/>) (Lucas, 2019). The wavelet analysis and Curie depth estimation were performed using the open-source software PlateCurie, freely available at (<https://github.com/paudetseis/PlateCurie>) (Audet & Gosselin, 2019). Tectonic ages of the southern Africa used with the permission of OneGeology (<http://portal.onegeology.org/OneGeologyGlobal/>). The resulting Curie depth and its uncertainties and the modelled heat flow can be found at (<https://doi.org/10.5281/zenodo.5070470>). All the used data and the modeling software are cited within the manuscript and listed in the references.

References

- Afonso, J. C., Salajegheh, F., Szwillus, W., Ebbing, J., & Gaina, C. (2019). A global reference model of the lithosphere and upper mantle from joint inversion and analysis of multiple data sets. *Geophysical Journal International*, 217(3), 1602–1628.
- Andrés, J., Marzán, I., Ayarza, P., Martí, D., Palomeras, I., Torné, M., ... Carbonell, R. (2018). Curie point depth of the Iberian peninsula and surrounding margins: a thermal and tectonic perspective of its evolution. *Journal of Geophysical Research: Solid Earth*, 123(3), 2049–2068.
- Audet, P., & Gosselin, J. M. (2019). Curie depth estimation from magnetic anomaly data: a re-assessment using multitaper spectral analysis and Bayesian inference. *Geophysical Journal International*, 218(1), 494–507. doi: 10.1093/gji/ggz166
- Begg, G., Griffin, W., Natapov, L., O'Reilly, S. Y., Grand, S., O'Neill, C., ... others (2009). The lithospheric architecture of Africa: Seismic tomography, mantle petrology, and tectonic evolution. *Geosphere*, 5(1), 23–50.
- Blakely, R. J. (1988). Curie temperature isotherm analysis and tectonic implications of aeromagnetic data from Nevada. *Journal of Geophysical Research: Solid Earth*, 93(B10), 11817–11832.
- Blakely, R. J., Brocher, T. M., & Wells, R. E. (2005). Subduction-zone magnetic anomalies and implications for hydrated forearc mantle. *Geology*, 33(6), 445–448.

- Botswana Geological Survey Department, Terra Surveys Ltd, & Canadian International Development Agency. (1978). *Reconnaissance aeromagnetic survey of botswana 1975-77: Final interpretation report*. Geological Survey Department, Republic of Botswana.
- Bouligand, C., Glen, J. M. G., & Blakely, R. J. (2009). Mapping Curie temperature depth in the western United States with a fractal model for crustal magnetization. *Journal of Geophysical Research*, 114(B11), B11104. doi: 10.1029/2009JB006494
- Campbell, I., Naldrett, A., & Barnes, S. (1983). A model for the origin of the platinum-rich sulfide horizons in the bushveld and stillwater complexes. *Journal of Petrology*, 24(2), 133–165.
- Catalán, M., Dymant, J., Choi, Y., Hamoudi, M., Lesur, V., Thébaud, E., ... others (2016). Making a better magnetic map. *EOS*.
- Celli, N. L., Lebedev, S., Schaeffer, A. J., & Gaina, C. (2020). African cratonic lithosphere carved by mantle plumes. *Nature communications*, 11(1), 1–10.
- Chopping, R., & Kennett, B. L. (2013). The curie depth of australia, and its uncertainty. *ASEG Extended Abstracts*, 2013(1), 1–3.
- Cornell, D. H., Van Schijndel, V., Ingolfsson, O., Scherstén, A., Karlsson, L., Wojtyła, J., & Karlsson, K. (2011). Evidence from dwyka tillite cobbles of archaean basement beneath the kalahari sands of southern africa. *Lithos*, 125(1-2), 482–502.
- Crameri, F., Shephard, G. E., & Heron, P. J. (2020). The misuse of colour in science communication. *Nature communications*, 11(1), 1–10.
- de Wit, M. J., Jones, M. G., & Buchanan, D. L. (1992). The geology and tectonic evolution of the pietersburg greenstone belt, south africa. *Precambrian Research*, 55(1-4), 123–153.
- Duncan, R. A., Hooper, P., Rehacek, J., Marsh, J., & Duncan, A. (1997). The timing and duration of the karoo igneous event, southern gondwana. *Journal of Geophysical Research: Solid Earth*, 102(B8), 18127–18138.
- Dunlop, D. J., & Özdemir, Ö. (2001). *Rock magnetism: fundamentals and frontiers* (No. 3). Cambridge university press.
- Ebbing, J., Dilixiati, Y., Haas, P., Ferraccioli, F., & Scheiber-Enslin, S. (2021). East antarctica magnetically linked to its ancient neighbours in gondwana. *Scientific reports*, 11(1), 1–11.
- Ebbing, J., Gernigon, L., Pascal, C., Olesen, O., & Osmundsen, P. T. (2009). A discussion of structural and thermal control of magnetic anomalies on the mid-norwegian margin. *Geophysical Prospecting*, 57(4), 665–681. doi: 10.1111/j.1365-2478.2009.00800.x
- Ebbing, J., Szwillus, W., & Dilixiati, Y. (2021). *A bayesian framework for simultaneous determination of susceptibility and magnetic thickness from magnetic data* (Tech. Rep.). Copernicus Meetings.
- Ellwood, B. B., Crick, R. E., Hassani, A. E., Benoist, S. L., & Young, R. H. (2000). Magnetosusceptibility event and cyclostratigraphy method applied to marine rocks: detrital input versus carbonate productivity. *Geology*, 28(12), 1135–1138.
- Ernst, R. E., Pereira, E., Hamilton, M. A., Pisarevsky, S. A., Rodrigues, J., Tassinari, C. C., ... Van-Dunem, V. (2013). Mesoproterozoic intraplate magmatic ‘barcode’ record of the angola portion of the congo craton: Newly dated magmatic events at 1505 and 1110 ma and implications for nuna (columbia) supercontinent reconstructions. *Precambrian Research*, 230, 103–118.
- Fadel, I., Paulssen, H., van der Meijde, M., Kwadiba, M., Ntibinyane, O., Nyblade, A., & Durrheim, R. (2020). Crustal and upper mantle shear wave velocity structure of botswana: The 3 april 2017 central botswana earthquake linked to the east african rift system. *Geophysical Research Letters*, 47(4), e2019GL085598.
- Fadel, I., van der Meijde, M., & Paulssen, H. (2018). Crustal structure and dynamics of botswana. *Journal of Geophysical Research: Solid Earth*, 123(12), 10–659.

- Ferré, E. C., Friedman, S. A., Martín-Hernández, F., Feinberg, J. M., Till, J. L., Ionov, D. A., & Conder, J. A. (2014). Eight good reasons why the uppermost mantle could be magnetic. *Tectonophysics*, 624-625, 3 - 14. (Crustal and mantle sources of magnetic anomalies)
- Gard, M., & Hasterok, D. (2021). A global curie depth model utilising the equivalent source magnetic dipole method. *Physics of the Earth and Planetary Interiors*, 313, 106672.
- Gaudreau, E., Audet, P., & Schneider, D. (2019). Mapping curie depth across western canada from a wavelet analysis of magnetic anomaly data. *Journal of Geophysical Research: Solid Earth*, 124(5), 4365-4385. doi: 10.1029/2018JB016726
- Goodwin, A. (1996). Principles of Precambrian Geology. Academic Press.
- Green, C., Barritt, S., Fairhead, J., & Misener, D. (1992). The african magnetic mapping project. In *Conference proceedings, 54th EAEG meeting, June 1992*. European Association of Geoscientists & Engineers.
- Haggerty, S. E. (1978). Mineralogical constraints on curie isotherms in deep crustal magnetic anomalies. *Geophysical Research Letters*, 5(2), 105-108.
- Hanson, R. (2003). Proterozoic geochronology and tectonic evolution of southern africa. *Geological Society, London, Special Publications*, 206(1), 427-463.
- Hanson, R. E., Crowley, J. L., Bowring, S. A., Ramezani, J., Gose, W. A., Dalziel, I. W. D., ... Mukwakwami, J. (2004). Coeval large-scale magmatism in the kalahari and laurentian cratons during rodinia assembly. *Science*, 304(5674), 1126-1129. doi: 10.1126/science.1096329
- Hasterok, D., & Chapman, D. (2011). Heat production and geotherms for the continental lithosphere. *Earth and Planetary Science Letters*, 307(1-2), 59-70.
- Hutchins, D., & Reeves, C. (1980). Regional geophysical exploration of the kalahari in botswana. *Tectonophysics*, 69(3), 201 - 220. doi: 10.1016/0040-1951(80)90211-5
- Jelsma, H. A., & Dirks, P. H. (2002). Neoarchaean tectonic evolution of the zimbabwe craton. *Geological Society, London, Special Publications*, 199(1), 183-211.
- Johnson, M., Van Vuuren, C., Visser, J., Cole, D., Wickens, H. d. V., Christie, A., & Roberts, D. (1997). The foreland karoo basin, south africa. In *Sedimentary basins of the world* (Vol. 3, pp. 269-317). Elsevier.
- Kaban, M. K., Tesauero, M., Mooney, W. D., & Cloetingh, S. A. P. L. (2014). Density, temperature, and composition of the north american lithosphere—new insights from a joint analysis of seismic, gravity, and mineral physics data: 1. density structure of the crust and upper mantle. *Geochemistry, Geophysics, Geosystems*, 15(12), 4781-4807. doi: 10.1002/2014GC005483
- Key, R. M., & Ayres, N. (2000a). The 1998 edition of the national geological map of botswana. *Journal of African Earth Sciences*, 30(3), 427-451.
- Key, R. M., & Ayres, N. (2000b). The 1998 edition of the national geological map of botswana. *Journal of African Earth Sciences*, 30(3), 427 - 451. (50th Anniversary of the Geological Survey) doi: 10.1016/S0899-5362(00)00030-0
- Kirby, J. F. (2005). Which wavelet best reproduces the fourier power spectrum? *Computers & Geosciences*, 31(7), 846-864. doi: 10.1002/2013JB010535
- Kirby, J. F., & Swain, C. J. (2014). The long-wavelength admittance and effective elastic thickness of the canadian shield. *Journal of Geophysical Research: Solid Earth*, 119(6), 5187-5214. doi: 10.1002/2013JB010578
- Lachenbruch, A. H. (1970). Crustal temperature and heat production: Implications of the linear heat-flow relation. *Journal of Geophysical Research*, 75(17), 3291-3300.
- Laske, G., Masters, G., Ma, Z., & Pasyanos, M. (2013). Update on crust1.0—a 1-degree global model of earth's crust. In *Geophys. res. abstr.* (Vol. 15, p. 2658).
- Leseane, K., Atekwana, E. A., Mickus, K. L., Abdelsalam, M. G., Shemang, E. M., & Atekwana, E. A. (2015). Thermal perturbations beneath the incipient okavango

- 846 rift zone, northwest botswana. *Journal of Geophysical Research: Solid Earth*,
847 *120*(2), 1210–1228.
- 848 Lesur, V., Hamoudi, M., Choi, Y., Dymant, J., & Thébault, E. (2016). Building the
849 second version of the world digital magnetic anomaly map (wdmam). *Earth, Plan-*
850 *ets and Space*, *68*(1), 1–13.
- 851 Li, C., Lu, Y., & Wang, J. (2017). A global reference model of curie-point depths
852 based on EMAG2. *Sci. Rep.*, *7*, 45129.
- 853 Lösing, M., Ebbing, J., & Szwillus, W. (2020). Geothermal heat flux in antarctica:
854 assessing models and observations by bayesian inversion. *Frontiers in Earth Sci-*
855 *ence*, *8*, 105.
- 856 Lucazeau, F. (2019). Analysis and mapping of an updated terrestrial heat flow
857 data set. *Geochemistry, Geophysics, Geosystems*, *20*(8), 4001–4024. doi: 10.1029/
858 2019GC008389
- 859 Martos, Y. M., Catalán, M., Jordan, T. A., Golynsky, A., Golynsky, D., Eagles, G.,
860 & Vaughan, D. G. (2017). Heat flux distribution of antarctica unveiled. *Geophysi-*
861 *cal Research Letters*, *44*(22), 11,417–11,426. doi: 10.1002/2017GL075609
- 862 Mather, B., & Delhaye, R. (2019). Pycurious: A python module for computing the
863 curie depth from the magnetic anomaly. *J. Open Source Softw.*, *4*(39), 1544. doi:
864 10.21105/joss.01544
- 865 Mather, B., & Fulla, J. (2019). Constraining the geotherm beneath the british isles
866 from bayesian inversion of curie depth: integrated modelling of magnetic, geother-
867 mal, and seismic data. *Solid Earth*, *10*(3), 839–850. doi: 10.5194/se-10-839-2019
- 868 Maus, S., & Dimri, V. (1996). Depth estimation from the scaling power spectrum of
869 potential fields? *Geophysical Journal International*, *124*(1), 113–120. doi: 10.1111/
870 j.1365-246X.1996.tb06356.x
- 871 Maus, S., Gordon, D., & Fairhead, D. (1997). Curie-temperature depth estima-
872 tion using a self-similar magnetization model. *Geophysical Journal International*,
873 *129*(1), 163–168. doi: 10.1111/j.1365-246X.1997.tb00945.x
- 874 McCourt, S., Hilliard, P., Armstrong, R., & Munyanyiwa, H. (2001). Shrimp u-pb
875 zircon geochronology of the hurungwe granite northwest zimbabwe: Age con-
876 straints on the timing of the magondi orogeny and implications for the correlation
877 between the kheis and magondi belts. *South African Journal of Geology*, *104*(1),
878 39–46.
- 879 Núñez, D., Prezzi, C., & Sánchez Bettucci, L. (2021). Review of curie point depth
880 determination through different spectral methods applied to magnetic data. *Geo-*
881 *phys. J. Int.*, *224*(1), 17–39. doi: 10.1002/2013EO450001
- 882 Olsen, N., Ravat, D., Finlay, C. C., & Kother, L. K. (2017). Lcs-1: a high-resolution
883 global model of the lithospheric magnetic field derived from champ and swarm
884 satellite observations. *Geophysical Journal International*, *211*(3), 1461–1477.
- 885 Olsson, J., Söderlund, U., Klausen, M., & Ernst, R. (2010). U–pb baddeleyite ages
886 linking major archean dyke swarms to volcanic-rift forming events in the kaapvaal
887 craton (south africa), and a precise age for the bushveld complex. *Precambrian*
888 *Research*, *183*(3), 490–500.
- 889 Pilkington, M., & Todoeschuck, J. P. (1993). Fractal magnetization of continental
890 crust. *Geophysical Research Letters*, *20*(7), 627–630. doi: 10.1029/92GL03009
- 891 Pollack, H. N., Hurter, S. J., & Johnson, J. R. (1993). Heat flow from the earth’s in-
892 terior: analysis of the global data set. *Reviews of Geophysics*, *31*(3), 267–280.
- 893 Pérez-Gussinyé, M., Swain, C. J., Kirby, J. F., & Lowry, A. R. (2009). Spatial varia-
894 tions of the effective elastic thickness, t_e , using multitaper spectral estimation and
895 wavelet methods: Examples from synthetic data and application to south america.
896 *Geochemistry, Geophysics, Geosystems*, *10*(4). doi: 10.1029/2008GC002229
- 897 Riley, T., Curtis, M., Leat, P., Watkeys, M., Duncan, R., Millar, I., & Owens, W.
898 (2006). Overlap of karoo and ferrar magma types in kwazulu-natal, south africa.
899 *Journal of Petrology*, *47*(3), 541–566.

- Roy, R. F., Blackwell, D. D., & Birch, F. (1968). Heat generation of plutonic rocks and continental heat flow provinces. *Earth and Planetary Science Letters*, 5, 1-12. doi: 10.1016/S0012-821X(68)80002-0
- Salem, A., Green, C., Ravat, D., Singh, K. H., East, P., Fairhead, J. D., ... Biegert, E. (2014). Depth to curie temperature across the central red sea from magnetic data using the de-fractal method. *Tectonophysics*, 624, 75-86.
- Scheiber-Enslin, S., Ebbing, J., & Webb, S. J. (2014). An integrated geophysical study of the beattie magnetic anomaly, south africa. *Tectonophysics*, 636, 228-243.
- Schmitz, M., & Bowring, S. (2003). Ultrahigh-temperature metamorphism in the lower crust during neoproterozoic rifting and magmatism, kaapvaal craton, southern africa. *Geological Society of America Bulletin*, 115, 533-548.
- Stettler, E., Fourie, C., & Cole, P. (2000). *Total magnetic field intensity map of the republic of south africa*. Council for Geoscience.
- Swain, C. J., & Kirby, J. F. (2003). The effect of 'noise' on estimates of the elastic thickness of the continental lithosphere by the coherence method. *Geophysical Research Letters*, 30(11). doi: 10.1029/2003GL017070
- Tanaka, A., Okubo, Y., & Matsubayashi, O. (1999). Curie point depth based on spectrum analysis of the magnetic anomaly data in east and southeast asia. *Tectonophysics*, 306(3-4), 461-470.
- Thomas, R., Von Veh, M., & McCourt, S. (1993). The tectonic evolution of southern africa: an overview. *Journal of African Earth Sciences (and the Middle East)*, 16(1-2), 5-24.
- Uieda, L., & Barbosa, V. C. F. (2017). Fast nonlinear gravity inversion in spherical coordinates with application to the south american moho. *Geophysical Journal International*, 208(1), 162-176. doi: 10.1093/gji/ggw390
- Van Schijndel, V., Cornell, D. H., Hoffmann, K.-H., & Frei, D. (2011). Three episodes of crustal development in the rehoboth province, namibia. *Geological Society, London, Special Publications*, 357(1), 27-47.
- Wang, J., & Li, C.-F. (2015). Crustal magmatism and lithospheric geothermal state of western north america and their implications for a magnetic mantle. *Tectonophysics*, 638, 112-125.
- Wasilewski, P. J., & Mayhew, M. A. (1992). The moho as a magnetic boundary revisited. *Geophysical Research Letters*, 19(22), 2259-2262. doi: 10.1029/92GL01997
- Wasilewski, P. J., Thomas, H. H., & Mayhew, M. A. (1979). The moho as a magnetic boundary. *Geophysical Research Letters*, 6(7), 541-544. doi: 10.1029/GL006i007p00541
- Wessel, P., Smith, W. H. F., Scharroo, R., Luis, J., & Wobbe, F. (2013). Generic mapping tools: Improved version released. *EOS, Transactions American Geophysical Union*, 94(45), 409-410. doi: 10.1002/2013EO450001
- White-Gaynor, A. L., Nyblade, A. A., Durrheim, R., Raveloson, R., van der Meijde, M., Fadel, I., ... Sitali, M. (2020). Lithospheric boundaries and upper mantle structure beneath southern africa imaged by p and s wave velocity models. *Geochemistry, Geophysics, Geosystems*, 21(10), e2020GC008925. doi: 10.1029/2020GC008925
- Witter, J., & Miller, C. (2017). Curie point depth mapping in yukon. *Yukon Geological Survey, Open File*, 3, 42.
- Wright, J. A., & Hall, J. (1990). Deep seismic profiling in the nosop basin, botswana: cratons, mobile belts and sedimentary basins. *Tectonophysics*, 173(1-4), 333-343.
- Youssof, M., Thybo, H., Artemieva, I., & Levander, A. (2013). Moho depth and crustal composition in southern africa. *Tectonophysics*, 609, 267 - 287. doi: 10.1016/j.tecto.2013.09.001

Supporting Information for ”Mapping the thermal structure of southern Africa from Curie depth estimates based on wavelet analysis of magnetic data with uncertainties”

M. Sobh¹, C. Gerhards¹, I. Fadel², and H.-J. Götze³

¹Institute of Geophysics and Geoinformatics, TU Bergakademie Freiberg, Germany

²Faculty of Geo-Information Science and Earth Observation, University of Twente, Enschede, Netherlands

³Institute of Geoscience, Christian-Albrechts-University Kiel, Otto-Hahn-Platz 1, D-24118 Kiel, Germany

Contents of this file

1. Figures S1 to S7

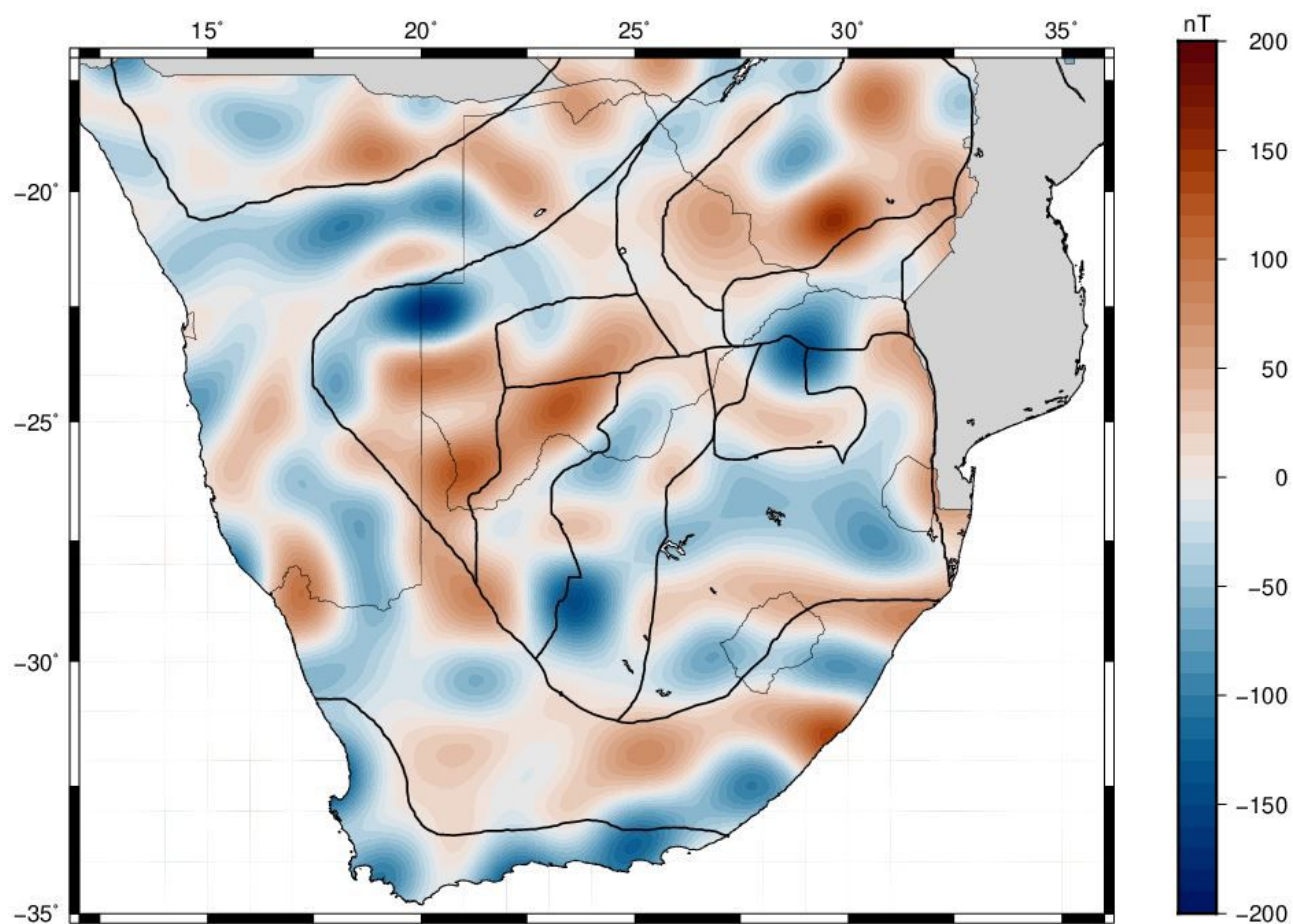


Figure S1. Lithospheric magnetic anomaly of Southern Africa derived from Satellite model LCS-1 (Olsen et al., 2017)

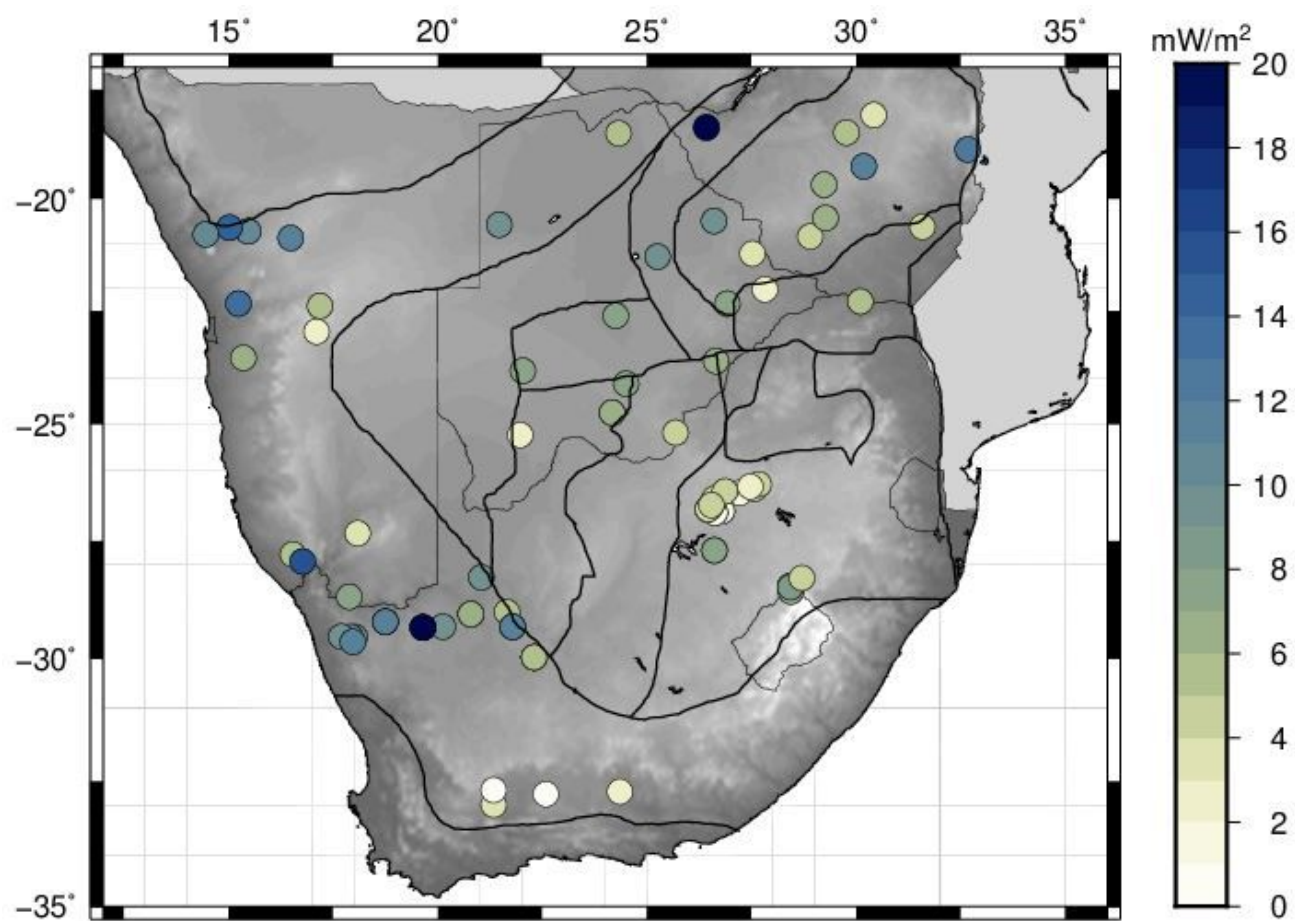


Figure S2. Uncertainty for the measured heat flow data (Lucazeau, 2019).

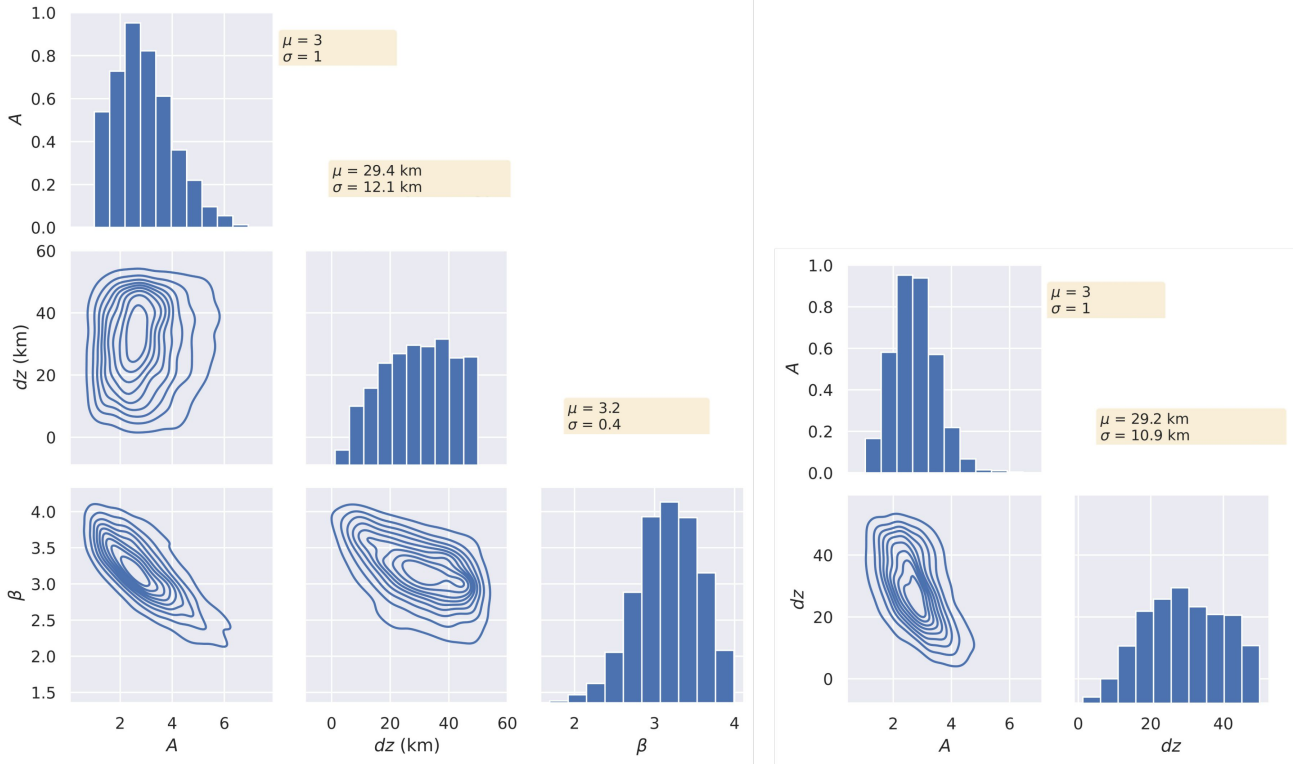


Figure S3. Statistical distribution of model parameters from at location B of Figure 5-a: marginalized and joint posterior distribution from the simultaneous inversion for the parameters z_b , β , and A (right panel) and for the simultaneous inversion for z_b and A , with fixed $\beta = 3.0$ (left panel). Statistical information on each z_b , β , A is provided in the orange boxes; μ is the mean value, σ is the standard deviation. Note that the parameter dz in the above plots indicates Δz in our notation, so that $z_b = z_t + dz$.

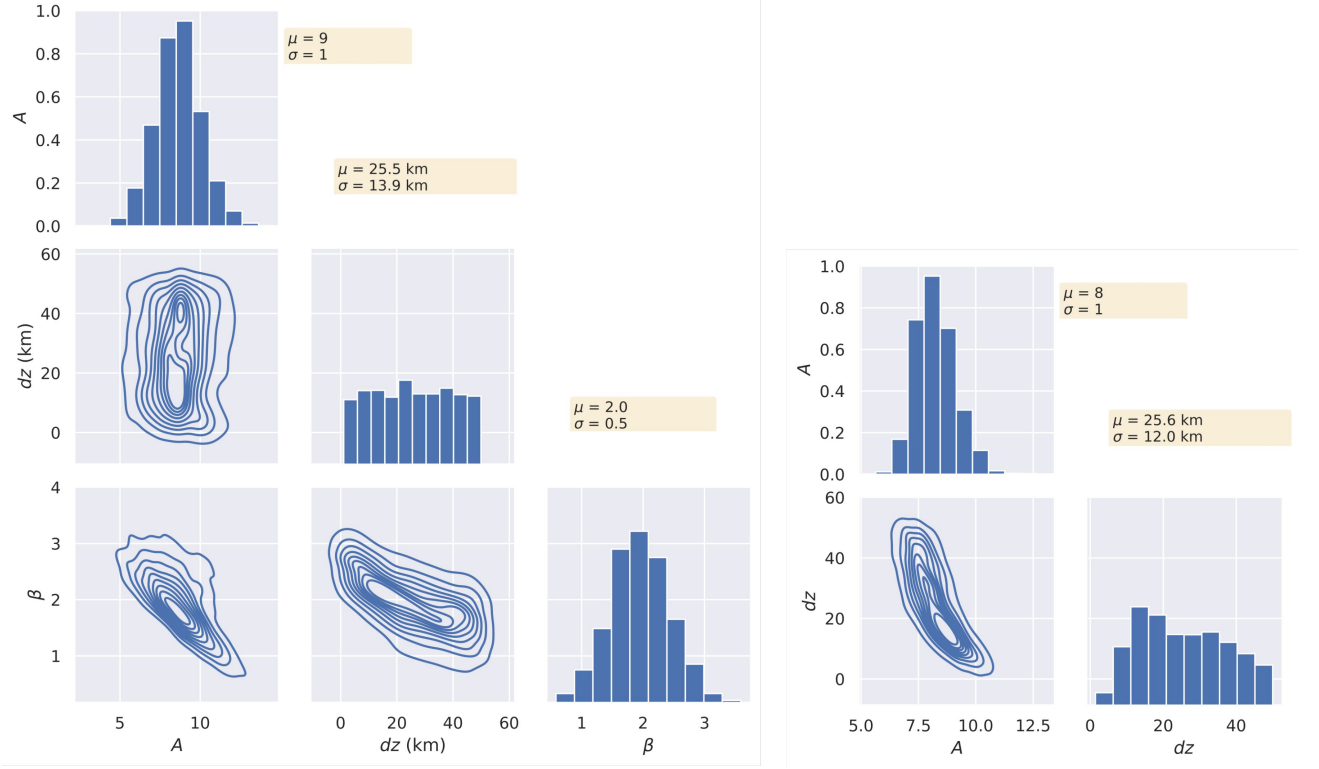


Figure S4. Statistical distribution of model parameters from at location C of Figure 5-a: marginalized and joint posterior distribution from the simultaneous inversion for the parameters z_b , β , and A (right panel) and for the simultaneous inversion for z_b and A , with fixed $\beta = 3.0$ (left panel). Statistical information on each z_b , β , A is provided in the orange boxes; μ is the mean value, σ is the standard deviation. Note that the parameter dz in the above plots indicates Δz in our notation, so that $z_b = z_t + dz$.

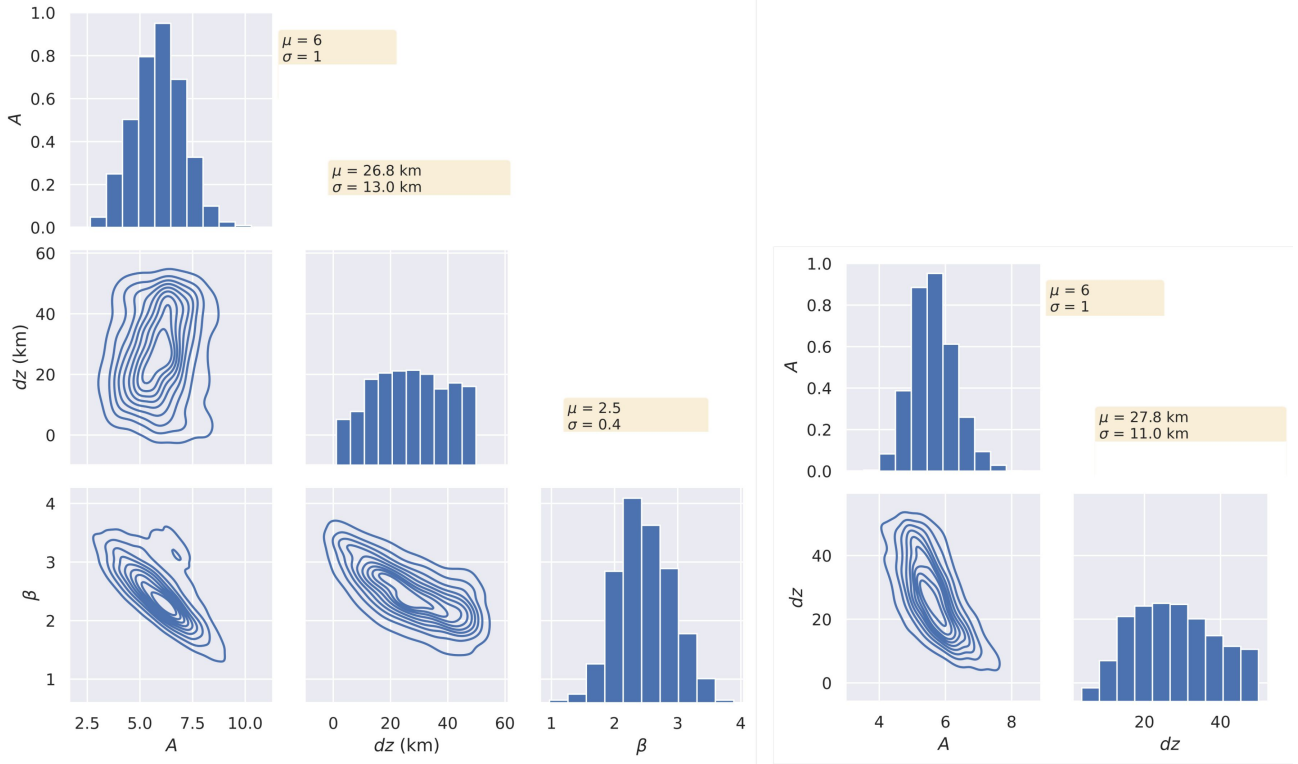


Figure S5. Statistical distribution of model parameters from at location D of Figure 5-a: marginalized and joint posterior distribution from the simultaneous inversion for the parameters z_b , β , and A (right panel) and for the simultaneous inversion for z_b and A , with fixed $\beta = 3.0$ (left panel). Statistical information on each z_b , β , A is provided in the orange boxes; μ is the mean value, σ is the standard deviation. Note that the parameter dz in the above plots indicates Δz in our notation, so that $z_b = z_t + dz$.

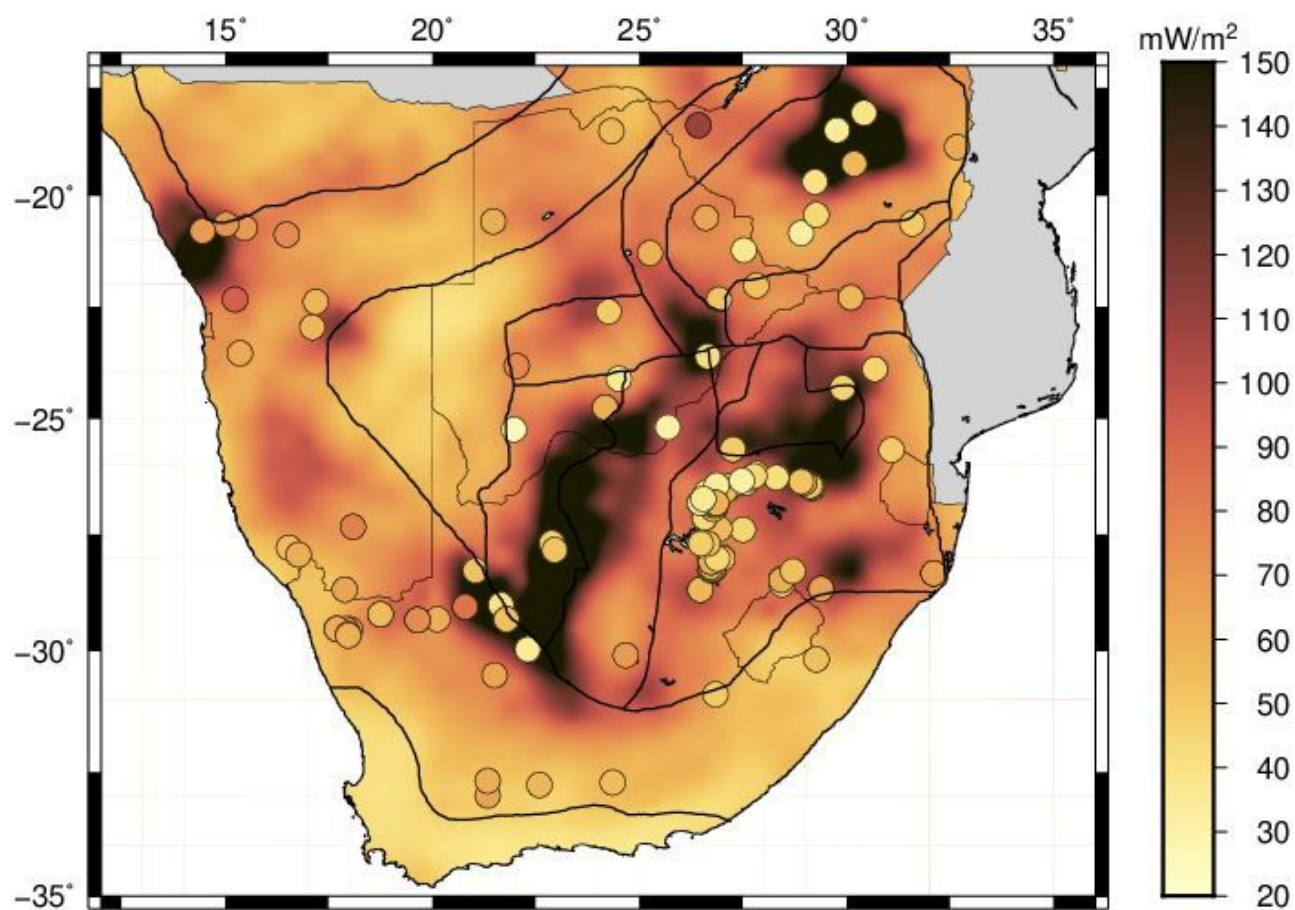


Figure S6. Heat flow distribution calculated from the global Curie depth model proposed by (Li et al., 2017) using laterally constant thermal conductivity ($k = 2.5 \text{ W/mK}$) overlain with the locations of the measured heat flow data.

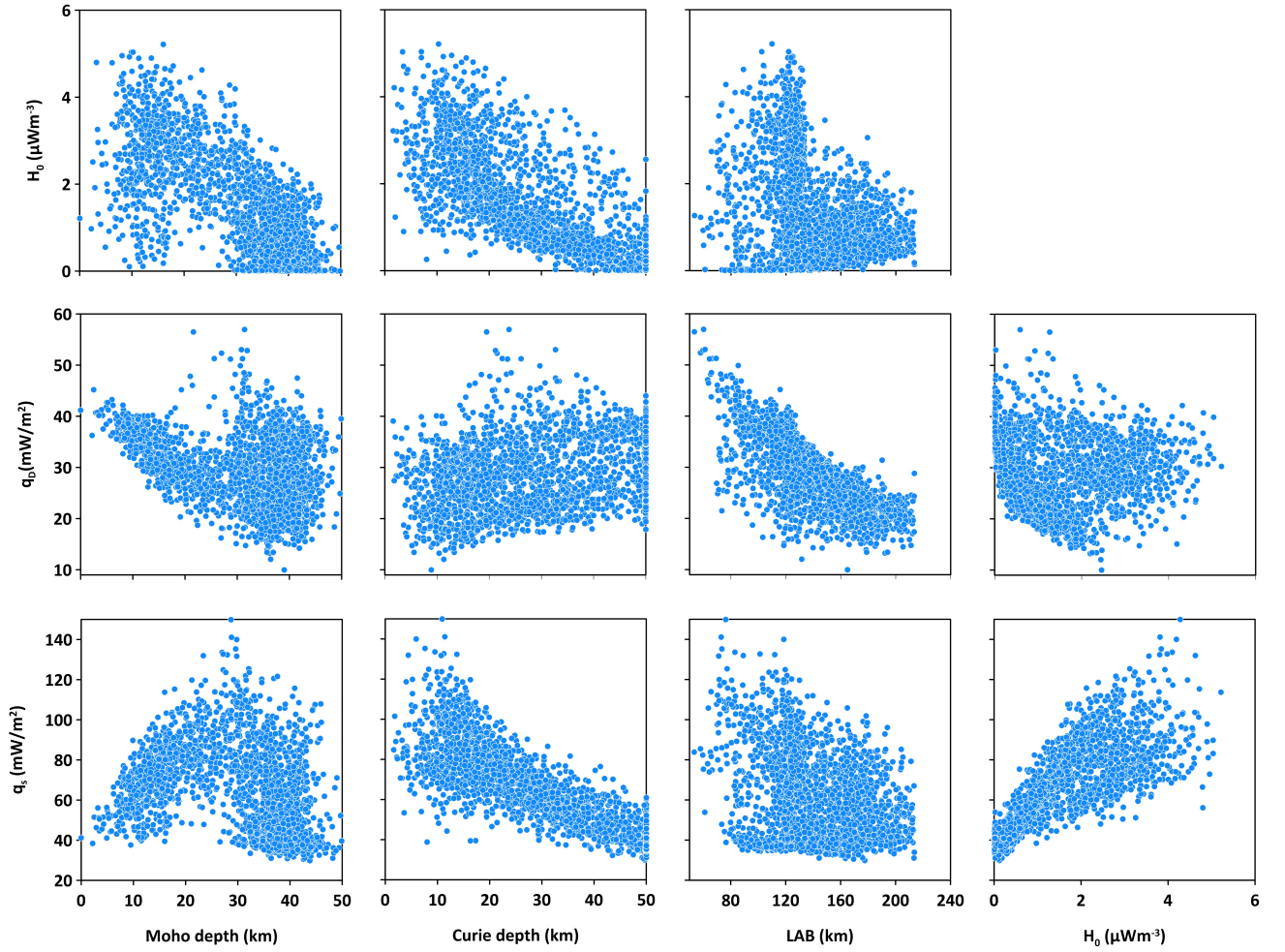


Figure S7. Correlations between different input and output parameters resulting from the heat flow modelling for a setup with varying thermal conductivities (cf. section 5.1.2 in the main text and (Lösing et al., 2020)) as a scatter plot. The figure shows a correlation between Curie depth with heat flow and heat production. LAB is correlated with mantle heat flux, and a linear correlation between heat flow and heat production is revealed.

References

- Li, C., Lu, Y., & Wang, J. (2017). A global reference model of curie-point depths based on EMAG2. *Sci. Rep.*, 7, 45129.
- Lösing, M., Ebbing, J., & Szwillus, W. (2020). Geothermal heat flux in antarctica: assessing models and observations by bayesian inversion. *Frontiers in Earth Science*, 8, 105.
- Lucazeau, F. (2019). Analysis and mapping of an updated terrestrial heat flow data set. *Geochemistry, Geophysics, Geosystems*, 20(8), 4001-4024. doi: 10.1029/2019GC008389
- Olsen, N., Ravat, D., Finlay, C. C., & Kother, L. K. (2017). Lcs-1: a high-resolution global model of the lithospheric magnetic field derived from champ and swarm satellite observations. *Geophysical Journal International*, 211(3), 1461–1477.